



Influence of alloying and surface overcoating engineering on the electrochemical properties of carbon-supported PtCu nanocrystals

Qiang Liu^{a,c,*}, Joseph Tripp^b, Claire Mitchell^b, Przemyslaw Rzepka^{a,c}, Ilia I. Sadykov^{c,d}, Arik Beck^{a,c}, Frank Krumeich^e, Srijita Nundy^b, Luca Artiglia^c, Marco Ranocchiari^c, Jeroen A. van Bokhoven^{a,c,*}

^a Department of Chemistry and Applied Biosciences, Institute for Chemical and Bioengineering, ETH Zurich, Vladimir Prelog Weg 1, 8093 Zurich, Switzerland

^b TFP Hydrogen Products Ltd., Unit 5 & 6, Merchants Quay, Pennygillam Industrial Estate, Launceston PL15 7QA, United Kingdom

^c Laboratory for Catalysis and Sustainable Chemistry, Paul Scherrer Institute, 5232 Villigen, Switzerland

^d Operando Spectroscopy Group, Paul Scherrer Institute, 5232 Villigen, Switzerland

^e Laboratory of Inorganic Chemistry, Institute for Chemical and Bioengineering, ETH Zurich, Vladimir Prelog Weg 1, 8093 Zurich, Switzerland

ARTICLE INFO

Keywords:

Alloying
Surface overcoating
Carbon nanoshells
Activity-stability trade-off
Pt-based electrocatalyst
Hydrogen evolution reaction

ABSTRACT

Designing nanostructured Pt-based materials with unique properties as electrocatalyst attracts great research interests to achieve clean and sustainable energy. Herein, we investigate nanoscale engineering of carbon-supported PtCu nanocrystals (NCs) through tailoring their electronic and geometry properties by means of alloying and surface overcoating. Alloying Pt with Cu enhances the catalytic efficiencies for the acidic hydrogen evolution reaction (HER). Subsequent surface overcoating of PtCu nanostructures with carbon nanoshells endows a decreased mass activity towards the HER catalysis compared to the uncoated counterparts, this can be mainly associated with annealing-induced sintering of small metal nanoparticles and the surface site-blockage of metal active sites. These results indicate that breaking activity-stability trade-off remains to be challenging for efficient HER catalysis on carbon-supported PtCu nanostructures. Our case study on the limitations of fabricating PtCu nanodendrites with varied loadings of carbon nanoshells on the surface demonstrates the necessity to explore the design of advanced and high-performing metal-based catalysts.

1. Introduction

Increasing concerns about climate change and fossil fuels depletion call for the use of green and sustainable energy [1]. Hydrogen represents a promising energy carrier due to its high energy density and zero-carbon emission [2]. An effective route for producing high-purity green hydrogen is the hydrogen evolution reaction (HER), a half-reaction taking place at the electrodes in devices such as water electrolyzers and H₂–Br₂ redox flow batteries (RFBs) [3–6]. Precious platinum (Pt) based materials are the state-of-the-art active HER catalysts [7]. Pt nanomaterials often suffer from catalytic degradation by nanoparticle (NP) dissolution, coalescence/sintering, or detachment from the support, which along with the high price and scarcity associated with the Pt metal, are obstacles preventing widespread application [8–11]. To this end, alloying Pt with earth-abundant transition metals, e. g., Cu, Fe, Co, Ni, has emerged as a promising alternative to reduce the

consumption of Pt and to enhance electrocatalytic performance [12–14]. Previous reports indicated that alloying Pt with 3d transition metals of smaller atomic radius could induce beneficial macrostrain effects as a result of Pt lattice contraction [15,16]. In addition, the *d*-band electronic structure of Pt can be modified through the ligand effects to modulate the sorption behavior of reactants and products at surface active sites [15,17]. PtCu alloyed materials with nanostructures such as core-shell [18], nanospheres [19,20], nanocubes [21,22], nanoframes [23–26] and nanodendrites [27,28] have been developed for catalyzing various electrochemical reactions. Most of these catalysts were prepared by wet chemical synthesis under high temperatures, with the presence of organic capping agents for nanoparticle size, shape and morphology control. As a consequence of the well-defined nanostructures, morphologies and atomic compositions, PtCu nanomaterials exhibit enhanced electrocatalytic HER performance compared to pure Pt counterparts [19,20,25,26,28].

* Corresponding authors at: Department of Chemistry and Applied Biosciences, Institute for Chemical and Bioengineering, ETH Zurich, Vladimir Prelog Weg 1, 8093 Zurich, Switzerland

E-mail addresses: qiang.liu@psi.ch (Q. Liu), jeroen.vanbokhoven@chem.ethz.ch (J.A. van Bokhoven).

<https://doi.org/10.1016/j.jalcom.2023.172128>

Received 19 June 2023; Received in revised form 3 September 2023; Accepted 10 September 2023

Available online 11 September 2023

0925-8388/© 2023 The Author(s). Published by Elsevier B.V. This is an open access article under the CC BY license (<http://creativecommons.org/licenses/by/4.0/>).

A widely explored strategy to enhance the electrocatalytic efficiencies, more especially the long-term durability of metal-based catalysts is overcoating the metal nanoparticles with protective overlayers [29]. Surface coating with overlayers, such as organic polymers [30–32], inorganic nanoshells [33,34], and metal oxides (e.g., SiO_2 and TiO_2) [35,36], can make the metal particles highly resistive towards aggregation, sintering and dissolution. Due to the excellent electrical conductivity, high chemical and structural stability, heteroatoms-doped carbon nanoshells are of broad interest for engineering advanced electrocatalysts [37–40]. Several methodologies involving synthetic deposition of carbon nanoshells onto metal particle surface have been developed. This includes the direct pyrolysis of metal-containing or metal-coordinated organic complexes under inert atmosphere [41,42] and chemical vapor phase deposition utilizing CH_3CN or acetylene as the carbon source [43,44]. In the presence of carbon nanoshells with elaborately controlled thickness [34] and graphitization degree [38], metal coalescence/sintering can be efficiently suppressed and the inner active sites remain permeable for reactants and electrolyte, thereby affording satisfactory electrocatalytic performance.

In this regard, the integration of carbon nanoshells with metal nanostructures might be a promising way to achieve more efficient electrocatalysts. Thus far, the versatility of surface overcoating with carbon nanoshells on the surface of PtCu nanostructures and the application of carbon-overcoated PtCu nanomaterial as a HER electrocatalyst have rarely been discussed. Herein, we investigate the electrochemical performance of PtCu alloyed nanomaterials with respect to the acidic hydrogen evolution reaction, by nanoscale engineering the nanomaterial's structural properties via metal alloying and surface overcoating. Carbon-supported porous PtCu nanocrystals (NCs), named as PtCu NCs/C, were synthesized by a facile colloidal reduction method at a moderate temperature (40 °C), yielding optimized composition and nanodendritic nanostructure. PtCu NCs/C catalysts exhibited markedly higher electrocatalytic activity and relatively good stability towards the acidic HER catalysis than a commercial Pt/C. Structural and electrocatalytic properties of PtCu NCs after overcoating of carbon overlayers, and the associated influences on the design of highly performing metal-based electrocatalysts are investigated and discussed in the present work.

2. Experimental section

2.1. Materials

Hexachloroplatinic(IV) acid hydrate ($\text{H}_2\text{PtCl}_6 \cdot x\text{H}_2\text{O}$, ~38% Pt basis), copper(II) chloride dihydrate ($\text{CuCl}_2 \cdot 2\text{H}_2\text{O}$, ≥99.95% trace metals basis), cobalt(II) nitrate hexahydrate ($\text{Co}(\text{NO}_3)_2 \cdot 6\text{H}_2\text{O}$, ACS reagent, ≥98%), nickel(II) nitrate hexahydrate ($\text{Ni}(\text{NO}_3)_2 \cdot 6\text{H}_2\text{O}$, 99.999% trace metals basis) and polyvinylpyrrolidone (PVP, average mol wt 40,000) were purchased from Sigma Aldrich. $\text{H}_2\text{PtCl}_6 \cdot x\text{H}_2\text{O}$ was prepared into 8 wt% aqueous solution and cautiously stored in a chemical fridge at around 4 °C for catalyst synthesis. L-Ascorbic acid (AA) was obtained from PanReac AppliChem ITW Reagents. Vulcan XC-72R carbon black was delivered by Cabot Corporation. Commercial Pt/C catalyst with 40 wt% of Pt loading was obtained from Alfa Aesar, Thermal Fisher Scientific. All the chemicals and materials were used as received.

2.2. Catalyst preparation

2.2.1. Synthesis of PtCu NCs

The PtCu NCs were prepared based on the method reported by Eid et al. with some modifications [45]. For the synthesis of Pt_4Cu NCs, 1.68 mL of 8 wt% $\text{H}_2\text{PtCl}_6 \cdot x\text{H}_2\text{O}$ and 4.5 mL 20 mM $\text{CuCl}_2 \cdot 2\text{H}_2\text{O}$ were firstly added into 15 mL H_2O with the presence of 0.2 g PVP. After the addition of 20 mL 0.1 M AA solution, the resulting suspension was sonicated at 40 °C for 3 h. Pt_4Cu NCs were collected by centrifuging at 9000 rpm for 40 min, followed by rinsing with 10 mL water/ethanol mixture (1/1,

v/v) to remove organic PVP and AA. After two consecutive rinsing/centrifugation processes, the product was re-dispersed in water by subjecting to ultrasonic treatment. Similarly, keeping the amount of CuCl_2 constant, Pt_3Cu and Pt_2Cu NCs were synthesized by adding 0.90 and 0.45 mL of $\text{H}_2\text{PtCl}_6 \cdot x\text{H}_2\text{O}$ solution, respectively. Pt NCs (named as Pt_4 NCs) were also prepared with the absence of CuCl_2 precursor in the solution by keeping the synthetic condition similar to that in the case of Pt_4Cu NCs.

2.2.2. Synthesis of carbon-supported PtCu NCs

Typically, 0.2 g carbon black (Vulcan XC-72R) was added into the aqueous dispersion containing PtCu NCs. After stirring at room temperature for 2 h, the mixture was centrifuged and vacuum-dried at 60 °C to obtain the carbon-supported PtCu NCs (denoted as PtCu NCs/C) with different Pt loadings. Pt and Cu compositions on the resulting materials were determined by inductively coupled plasma optical emission spectrometry (ICP—OES). All PtCu NCs/C samples possess relatively lower Pt/Cu atomic ratios than the synthetic values and are, hereinafter, referred to as $\text{Pt}_4\text{Cu/C}$, $\text{Pt}_3\text{Cu/C}$ and $\text{Pt}_2\text{Cu/C}$. The Pt weight loadings on $\text{Pt}_4\text{Cu/C}$, $\text{Pt}_3\text{Cu/C}$ and $\text{Pt}_2\text{Cu/C}$ were determined to be 20 wt%, 10 wt% and 5.3 wt%, while that of Cu was 1.6 wt%, 1.1 wt% and 0.95 wt%, respectively. These values show that the PtCu NCs are formed by the co-reduction of Pt and Cu precursors by AA and the deposition process of Cu cation on Pt nuclei can be influenced by Pt concentrations in the synthetic solution. $\text{Pt}_4\text{Cu/C-700}$ and $\text{Pt}_2\text{Cu/C-700}$ were obtained after directly annealing at 700 °C without mixing with PVP and AA organics.

2.2.3. Overcoating of PtCu NCs with carbon nanoshells

Organic PVP and AA employed for the colloidal synthesis of PtCu NCs were utilized as the source of carbon nanoshells. $\text{Pt}_4\text{Cu/C}$ and $\text{Pt}_2\text{Cu/C}$ were selected to explore the effects of carbon overcoatings on their nanostructural properties and the corresponding electrocatalytic HER performance. Resulting catalysts were named as $\text{Pt}_4\text{Cu@C-m-700}$ and $\text{Pt}_2\text{Cu@C-m-700}$, where m represents the loading of PVP and AA organics on PtCu NCs/C prior to the pyrolysis treatment at 700 °C. In a typical preparation of $\text{Pt}_4\text{Cu@C-100%-700}$, 20 mg of $\text{Pt}_4\text{Cu/C}$ was mixed into 1 mL aqueous solution containing 16 mg PVP and 28 mg AA, followed by the vacuum drying at 70 °C overnight. After being ground in a mortar, the powder was thermally annealed at 700 °C in a tube furnace under flowing N_2 (50 cm^3/min) for 5 h. This process was started at room temperature with a heating rate of 5 °C/min and ended with a cooling down step to room temperature. $\text{Pt}_4\text{Cu@C-30%-700}$ and $\text{Pt}_4\text{Cu@C-60%-700}$ were prepared by using the aqueous solutions containing decreased concentrations of PVP and AA (30% and 60% of the total amount (16 mg PVP + 28 mg AA)). In analogy to $\text{Pt}_4\text{Cu@C-m-700}$, a set of $\text{Pt}_2\text{Cu@C-m-700}$ materials were obtained by changing the loadings of PVP and AA (e.g., 30%, 60%, 100%, 200% with respect to the amount (8.3 mg PVP + 14 mg AA) used for Pt_2Cu NCs synthesis), followed by the treatment of high-temperature pyrolysis.

2.3. Catalyst characterizations

Bright field transmission electron microscopy (TEM) images were obtained on FEI Tecnai F30 operated at 300 kV. Scanning transmission electron microscope (STEM) and energy dispersive X-ray (EDX) mapping analysis were performed on a probe-corrected Hitachi HD2700CS with an accelerating voltage of 200 kV (cold field emitter). An aberration corrector (CEOS) was incorporated in the microscope column between the condenser system and the probe-forming objective lens to achieve a high resolution of ca. 0.1 nm. Powder X-ray diffraction (XRD) measurements were carried out ex situ in the 2θ range of 10–90° on Bruker D8 advance, using $\text{Cu K}\alpha$ radiation ($\lambda = 0.15406$ nm) as the X-ray source. Fine-ground catalyst powder was loaded on a sample holder as a thin layer and rotary scanned with an increment step of 0.02° (for PtCu NCs/C catalysts otherwise specially noted) or 0.05° by keep the time/step of 5 s. The refinement of face centered cubic (fcc) Pt lattice was

performed with TOPAS 7 software simultaneously against the all subsequent datasets. The peak profile and instrumental peak broadening were determined beforehand with Pseudo-Voigt function fitted to data collected from the corundum (Al_2O_3) internal standard. The integral breadth of Bragg reflections evaluated by fitting Lorentzian function to the data enabled deriving the crystalline size. ICP—OES analysis was conducted on a Horiba Ultra 2 instrument with a photomultiplier tube detector. Thermal gravimetric analysis (TGA) was carried out on the NETZSCH STA 449 C thermal analyzer by heating the mixture of $\text{Pt}_4\text{Cu}/\text{C}$ with 100% organics (40.8 mg in total) up to 700°C with a heating rate of $5^\circ\text{C}/\text{min}$ under a N_2 atmosphere. X-ray photoelectron spectroscopy (XPS) and X-ray absorption spectra (XAS) was recorded at the in situ Spectroscopy (X07DB) beamline and the SuperXAS beamline, respectively, at the Swiss Light Source synchrotron (PSI, Villigen, Switzerland). For the details of XPS and XAS measurements and the corresponding data processing, please see from the [supporting information](#).

2.4. Electrochemical measurements

All the electrochemical measurements were conducted in a three-electrode cell system at room temperature. The cell is composed of a graphite rod as the counter electrode, reversible hydrogen electrode as a reference electrode, and a working electrode. All the potentials in the present work are reported versus the reversible hydrogen electrode (RHE). The working electrode was fabricated by coating Pt-based catalyst onto a glassy carbon electrode (GCE) having 5 mm in diameter (area: 0.196 cm^2). Typically, catalyst ink was prepared by ultrasonically suspending 2 mg of catalyst powder in 1 mL mixture of iso-propanol/water (3.98/1, v/v) with 5% w/w Nafion™ D-520. Then 10 μL catalyst ink was introduced onto the GCE and dried at room temperature. Nafion ionomer serves not only as a catalyst binder, but also as the promotor of proton conductivity. The mass loading for Pt-based catalysts on the electrode is 0.02 mg, otherwise specially noted.

HER measurements were performed in N_2 -saturated 0.5 M H_2SO_4 solution. The HER polarization curves were collected without IR compensation by sweeping the potential from + 0.7 to − 0.3 V vs. RHE

with a rate of 10 mV/s. Catalyst electrochemical stability was evaluated by cycling the potential (between +0.3 and −0.3 V vs. RHE) at a rate of 10 mV/s for 500 cycles. The cyclic voltamogram (CV) was obtained by cycling between 0.05 and 1.2 V vs. RHE with a scan rate of 20 mV/s in N_2 -saturated 0.1 M HClO_4 solution. Electrochemical surface area (ECSA) was calculated based on the following equation: $\text{ECSA} = Q_{\text{H}}/([m] \times 0.21)$, where Q_{H} (mC) is the integrated hydrogen desorption charge in the range of 0.05–0.40 V vs. RHE, 0.21 (mC/ cm^2) is the required charge for hydrogen monolayer adsorption, and $[m]$ (mg) represents as the loading amount of metal on the working electrode. Double-layer capacitance (C_{dl}) within the range of + 0.46 to + 0.26 V vs. RHE was measured with the sweep rate from 5 to 40 mV/s.

3. Results and discussions

3.1. Structural characterizations and catalytic HER performance of PtCu NCs/C

3.1.1. Electrocatalyst synthesis and characterization

The PtCu NCs were wet-chemically synthesized through co-reduction of H_2PtCl_6 and CuCl_2 in the presence of polyvinylpyrrolidone (PVP) and L-Ascorbic acid (AA) under an ultrasonic condition, as schematically illustrated in Fig. 1. The ultrasonic treatment was effective for accelerating the reduction of Pt and Cu cations to form PtCu NCs [45]. It was visually implied by the fast color change - within in 15 min - of the solution from transparent yellow to brown and opaque black (Fig. S1). There was no color change within one hour for a solution containing H_2PtCl_6 but without CuCl_2 treated at the same conditions. The Cu^{2+} could not be reduced by AA even after three hours in the absence of the Pt precursor in the solution (Fig. S1). Previous reports indicate the different reductive capability of AA for Pt and Cu precursors as function of the standard reduction potential of $\text{PtCl}_6^{2-}/\text{Pt}$ (0.74 V vs. RHE) and Cu^{2+}/Cu pair (0.34 V vs. RHE) [46,47]. Due to its higher standard reduction potential, the Pt precursor can be reduced by AA to form Pt nuclei at the early stage of the synthesis under an ultrasonic condition [27,45]. Metal underpotential deposition (UPD) takes place at hundreds

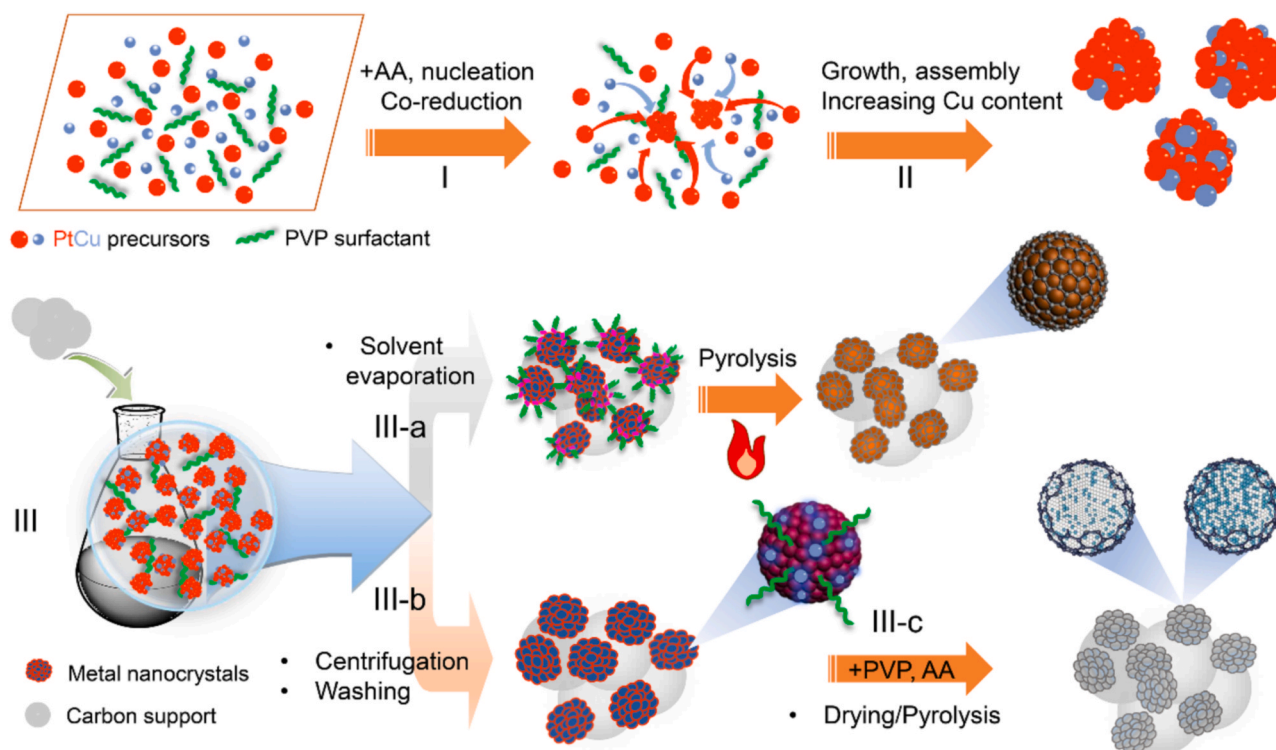


Fig. 1. Schematic illustration of the preparation of carbon-supported PtCu nanocatalysts.

of mVs more positive than the potential for its bulk deposition, as is known to be an effective approach to prepare alloyed metal catalysts in the presence of weak reducing agents [48,49]. The initial nucleation of Pt induces Cu UPD on their surface and the formation of PtCu nanocrystals can be promoted by the simultaneous co-reduction of Pt and Cu cations. PVP, as a stabilizing and structure-directing agent, is able to coordinate with metal atoms on the surface of metal nuclei through the carbonyl group and pyrrolidone ring to control the particle growth [50] and facilitate the formation of PtCu NCs with unique nanostructures through the process of growth rather than aggregation [45,51].

The nanostructures of PtCu NCs/C samples were investigated by STEM. The Z-contrast STEM images of Pt₄Cu/C and Pt₂Cu/C in Fig. 2a and d show that PtCu NCs (bright patches) are dispersed on the carbon black material. Fig. 2b and e display the Z-contrast, secondary electron (SE) and bright field (BF) images of a single PtCu nanocrystal on Pt₄Cu/C and Pt₂Cu/C. Small-sized PtCu NPs are recognizable from the PtCu agglomerates, as evidenced by the SE images. BF-STEM (Fig. 2b and e, bottom) and Z-contrast STEM images (Fig. 2c and f) show that PtCu NCs on Pt₄Cu/C are composed of a number of small-sized PtCu NP (averaged 2 nm in diameter) with a close contact. The PtCu NCs on Pt₂Cu/C are more loosely packed. The size determination gives rise to an averaged diameter of the agglomerates of ca. 30 and 20 nm for PtCu NCs on Pt₄Cu/C and Pt₂Cu/C, respectively. In the EDX mappings of Pt and Cu (Fig. 2c and f), the bright patches prove the presence of corresponding metals and they almost appear at the same sites, indicating the formation of PtCu alloys that are highly distributed on PtCu NCs/C. The greater intensity of the patches for Pt (green color) comparing to that of Cu (red color) is due to the higher loading of Pt than Cu on the carbon support. Figs. S2 and S3 show the EDX spectra of Pt₄Cu/C and Pt₂Cu/C with the atomic ratio of Pt to Cu determined to be about 79/21 and 66/34, respectively, which is in line with the results measured by ICP-OES.

The structures of PtCu NCs/C were also identified by XRD measurements. Pt₄Cu/C and Pt₄/C clearly display four reflections assigned

to (111), (200), (220) and (311) planes of a face-centered cubic (fcc) structure of Pt [52], as shown in Fig. 3a. Only the (111) reflections are observed from the Pt₃Cu/C and Pt₂Cu/C samples. Relative to the pattern of Pt₄/C, the (111) reflection peak shows a gradual shift (i.e., from 39.93° for Pt/C to 40.426° for Pt₂Cu/C) towards a higher angle with changes of metal loading. This indicates the incorporation of Cu atoms into the Pt lattice and the subsequent formation of the PtCu alloy-structured phase [20]. The occurrence of alloy phase can be confirmed by the refined lattice parameters of PtCu NCs/C; e.g., Pt₄Cu/C sample possesses a lattice parameter (3.8828 Å) which is more closer to the value (3.92 Å) of Pt reference than Cu reference (3.61 Å). Based on the refined lattice parameters for Pt₄Cu/C (3.8828 Å) and Pt₂Cu/C (3.856 Å), their Pt to Cu atomic ratio was calculated to be 89/11 and 80/20, respectively, by using the Vegard's law equation (Equation S1, supporting information). Comparing to the results from EDX and ICP-OES, obvious deviations from Vegard's law were observed for Cu composition. Pt-based nanoalloys with transition metals such as Cu, Fe, Co, Ni, have been reported to seldom perfectly obey the Vegard's law, due to the compressive stresses as a result of the differences in metal atomic size and unit cell volume (e.g., Cu: 11.8 Å³; Pt: 15.8 Å³) [53]. The broad reflection at 2θ of 10–30° is indexed to the (002) peak of graphitic carbon support [54].

The surface composition and chemical state of PtCu NCs/C were detected by means of XPS. High-resolution Pt 4f XPS spectra for Pt₄Cu/C is plotted in Fig. 3b. It is clear that Pt with a zero-valence is dominant (more than 68% of atomic composition) on PtCu NCs, showing the doublet peaks with binding energies (BEs) at 71.2 and 74.5 eV [55]. The second deconvoluted doublet pairs centered at 72.6 and 75.8 eV are ascribed to ionic Pt²⁺ surface species [56]. Pt 4f photoemission peaks for Pt₄Cu/C (Fig. 3b) and Pt₂Cu/C (Fig. S4) shift to a slightly higher BE than that (70.9–71.0 eV for 4f_{7/2}, 74.2–74.3 eV for 4f_{5/2}) of reference bulk Pt [57–59]. This shift of Pt 4f binding energy by 0.2–0.3 eV in the present study is probably a result of the small particle size of PtCu and

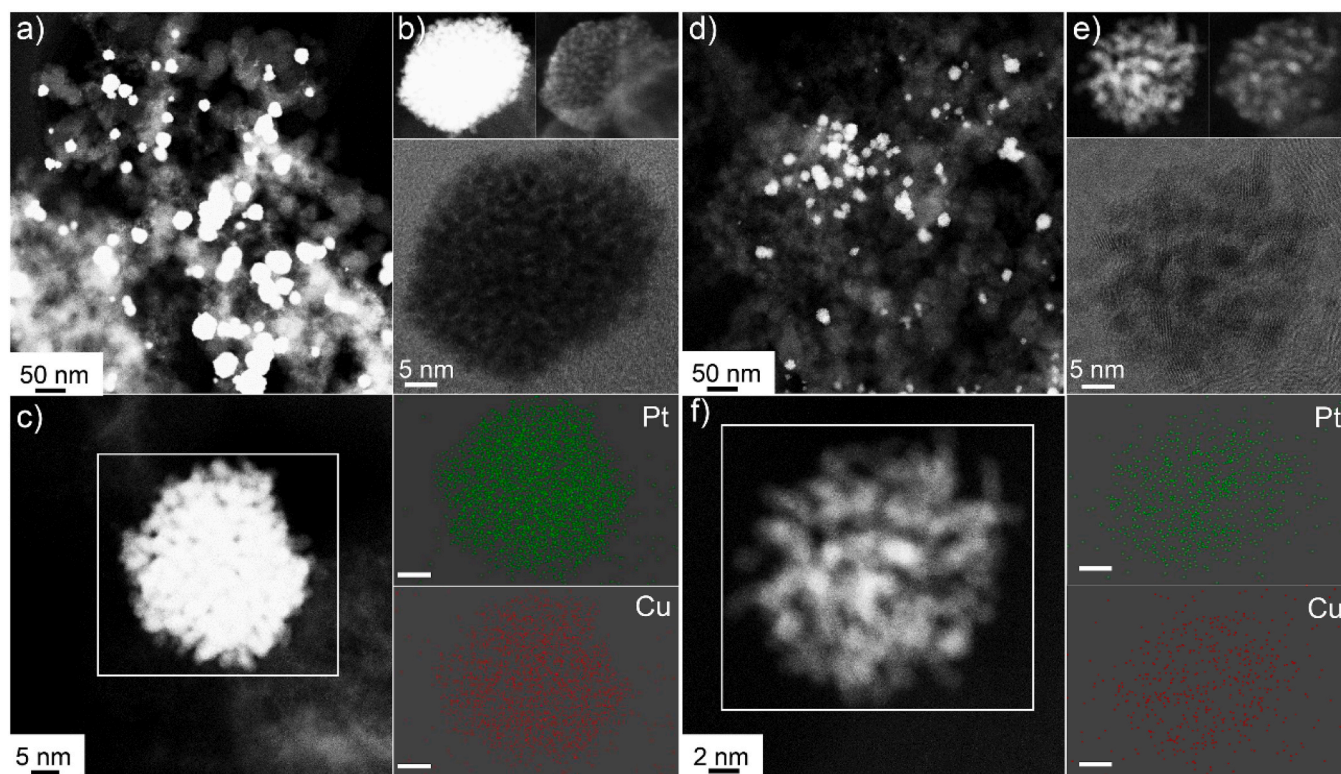


Fig. 2. Z-contrast STEM images of (a) Pt₄Cu/C and (d) Pt₂Cu/C. Z-contrast, secondary electron and bright field images of single PtCu nanocrystal on (b) Pt₄Cu/C and (e) Pt₂Cu/C. EDX elemental mapping of Pt (green color) and Cu (red color) of a PtCu nanocrystal on (c) Pt₄Cu/C and (f) Pt₂Cu/C. All the scale bars, instead of those (5 nm in (c) and 2 nm in (f)) of EDX mapping images, are presented in the STEM images.

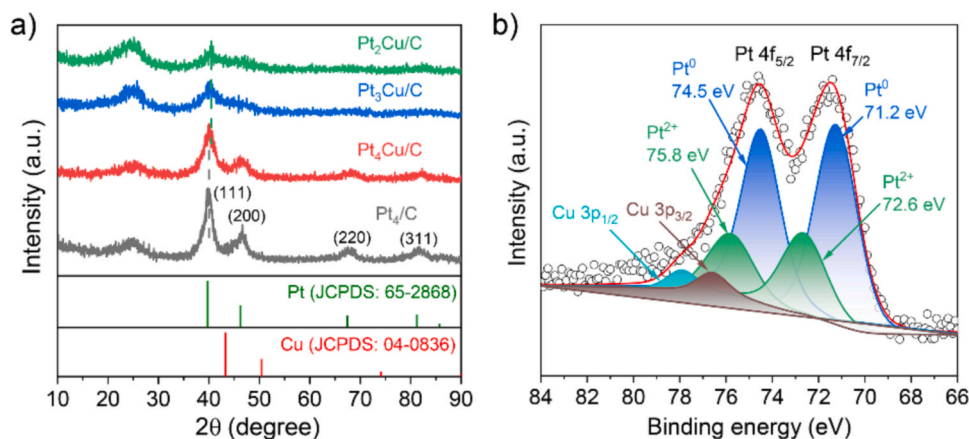


Fig. 3. (a) XRD patterns of Pt₄Cu/C, Pt₃Cu/C, Pt₂Cu/C and Pt₄/C with the standard X-ray diffraction lines of metallic Pt and Cu plotted below. (b) The high-resolution Pt 4f XPS spectra for Pt₄Cu/C sample.

their interactions with the carbon support [58,60]. In addition, the two deconvoluted broad XPS peaks with the BEs at 76.6 and 77.9 eV are related to Cu 3p_{3/2} and Cu 3p_{1/2}, respectively [61]. Concerning the deconvolution of Cu 2p spectra (Fig. S4), it was not possible to discriminate Cu⁰ from Cu⁺ because of their overlap in the Cu 2p signal [60]. Despite the low signal to noise ratio due to the low amount of Cu, it is possible to identify two main components in the 2p_{3/2} at 931.3 and 932.5 eV, attributed to Cu alloyed with Pt and Cu⁰/Cu⁺ sites on the surface, respectively [62,63]. Compared to the BE assigned in the literature to metallic Cu (932.8 eV) [55], the peak for the Cu⁰/Cu⁺ sites detected in Pt₄Cu/C sample shows a BE value smaller by 0.3–0.6 eV. From the Cu 2p spectra of Pt₄Cu/C (Fig. S4a,b), the peaks related to the Cu²⁺ species with higher BE region of 934–935 eV was not observed. Analysis of the surface composition of Pt₄Cu/C showed the Pt to Cu atomic ratio of (3.7 ± 0.1)/1, which is similar to the bulk ratio of 4/1 that was indicated by ICP–OES. In addition, a ratio of 66.8%:33.2% for Pt⁰/Ptⁿ⁺ and 7.5%:92.5% for Cu²⁺/(Cu⁰ + Cu⁺ + Cu_{alloy}) were determined for Pt₄Cu NCs. In the case of Pt₂Cu/C, the Cu 2p spectra was mainly deconvoluted into peaks assigning to Cu_{alloy} (931.4 and 951.1 eV), Cu⁰/Cu⁺ (932.2 and 952.0 eV) and Cu²⁺ sites (934.5 and 954.8 eV) (Fig. S4). The shakeup satellite peaks with much lower intensities at higher BEs (i.e., 942 and 962.2 eV) were also identified [64, 65]. Moreover, Pt and Cu with both metallic and oxidized states coexist in the Pt₂Cu/C sample, showing a ratio of 76.8%:23.2% for Pt⁰/Ptⁿ⁺ and 32.8%:67.2% for Cu²⁺/(Cu⁰ + Cu⁺ + Cu_{alloy}). The determination of the Pt and Cu species with different surface compositions indicate the unique nanostructures of Pt₄Cu and Pt₂Cu NCs supported on the carbon material.

3.1.2. HER performance of PtCu NCs/C

The CV curves of Pt₄Cu/C, Pt₃Cu/C, Pt₂Cu/C and commercial 40% Pt/C (abbreviated as Comm. Pt/C) are shown in Fig. S5. Hydrogen underpotential deposition (H_{upd} , 0–0.4 V vs. RHE), a double-layer region (0.4–0.7 V vs. RHE) and Pt oxidation/reduction region (0.7–1.0 V vs. RHE) were identified from the collected CV curves. The ECSA values of the surface active sites were calculated by integrating the charges obtained from the H_{upd} region [46], showing an decreasing trend: Comm. Pt/C (50 m²/g_{Pt}) > Pt₄Cu/C (39 m²/g_{Pt}) > Pt₃Cu/C (27 m²/g_{Pt}) > Pt₂Cu/C (15 m²/g_{Pt}). All the PtCu NCs/C materials possess lower values of ECSA relative to the reference Pt/C, likely arising from the formation of large PtCu aggregates. Their HER catalytic properties were examined in a N₂-saturated 0.5 M H₂SO₄ solution at room temperature. Fig. 4a shows the HER polarization curves without IR compensation. The overpotentials needed to deliver the current density of 10 and 50 mA/cm² for Pt₄Cu/C, Pt₃Cu/C and Pt₂Cu/C were lower than those of Pt₄/C and Comm. Pt/C (Fig. 4b). Determining of the Tafel slope of these

catalysts based on linear sweep voltammetry is impossible, since Tafel analysis is overpotential-dependent and must be in a steady state, irrespective of how low the scan rate is [66]. The use of various steady-state polarization techniques such as potentiostatic or galvanostatic responses for Tafel analysis has been strongly recommended [66,67]. To avoid causing any misleading, the Tafel slope values are not shown in this work. The mass activities of PtCu NCs/C at the overpotential of 50 and 100 mV are compiled in Fig. 4b. In particular, Pt₂Cu/C exhibits the highest mass activity of 6.4 A/mg_{Pt}, which is 6–10 times larger than determined for Pt₄/C (1.0 A/mg_{Pt}) and Comm. Pt/C (0.6 A/mg_{Pt}) at 50 mV of overpotential. The enhanced electrocatalytic HER activity of PtCu NCs/C was associated to the unique porous nanostructures of the PtCu NCs, which are favorable for the charge and mass transfer processes on catalyst's surface [68]. Besides, the incorporation of Cu into Pt lattice could bring out modified electronic structures and the synergetic effect that facilitates the affinity of intermediate hydrogen species and their recombination on the PtCu surface for enhanced HER catalysis [25].

Electrocatalytic stability is one of the most important criteria for the practical application of supported metal catalysts. The catalytic HER stability of Pt₄Cu/C and Pt₂Cu/C was assessed by comparing with the reference Comm. Pt/C. After continuous 500 cycles in N₂-saturated H₂SO₄ solution, the overpotentials at 10 mA/cm² of current density for PtCu NCs/C samples were positively increased by nearly 18 mV (Fig. 4c). In the case of Comm. Pt/C, a shift of 14 mV for the overpotential was estimated under the similar condition. The Pt₂Cu/C catalyst with a Pt loading of 5.3 wt% has been observed to possess the highest mass activity and a relatively good stability, thus making it promising to decrease Pt consumption while maintaining high-performance electrocatalysis. STEM measurement on Pt₂Cu/C (Fig. S6) revealed the unchanged morphology of PtCu nanodendrites that are remained to be highly dispersed on carbon support after the long-term stability test.

Metal nanoparticle dissolution, detachment from the carbon support and aggregation/sintering constitute the major origins of the low stability of Pt-based catalysts in acidic electrolytes [9]. Owing to the difference in atomic size and reduction potential of Pt and Cu, the dissolution of Cu atoms from the PtCu NCs would become favorable in order to reduce the compressive stresses on Pt atoms [53]. The fast dissolution of Cu was confirmed by the evaluations of the chemical stability of PtCu-based catalysts after immersing them into 0.5 M H₂SO₄ solution for 48 h without applying a potential (Fig. S7). Due to the detection limit of ICP–OES, performing elemental analysis on the electrolyte after the 500 cycles testing to determine the dissolution amount of Pt and Cu is practically impossible. However, the (chemical and/or electrochemical) dissolution of metals, in particular, Cu from

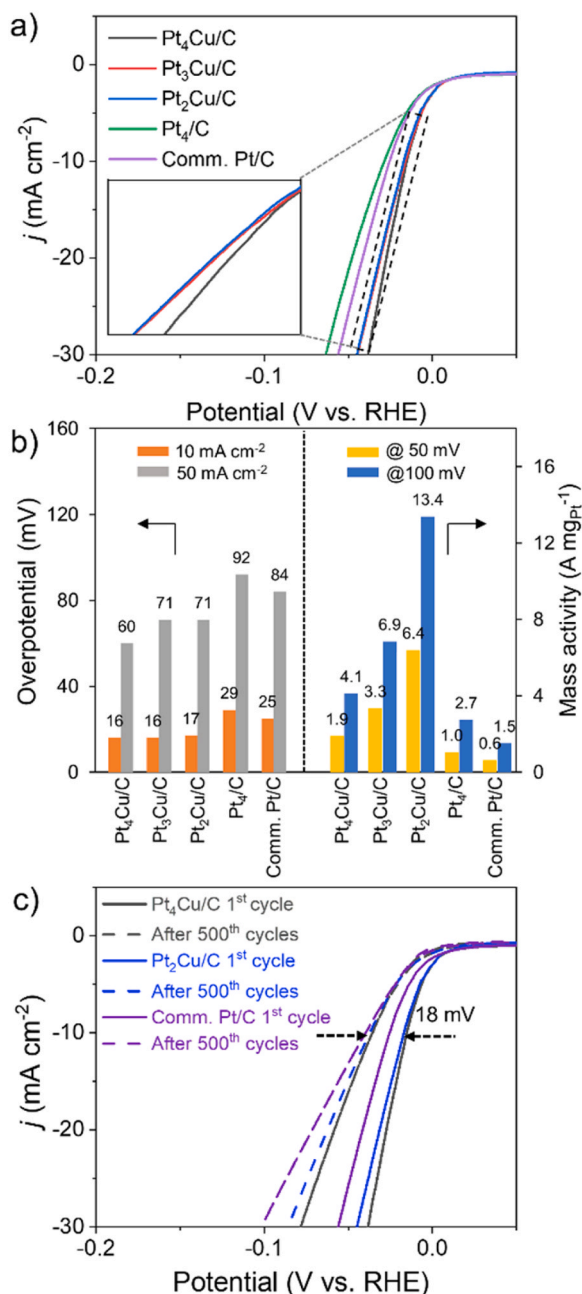


Fig. 4. HER performance of Pt₄Cu/C, Pt₃Cu/C, Pt₂Cu/C, Pt₄/C and commercial Pt/C in 0.5 M H₂SO₄ electrolyte. (a) HER polarization curves, (b) overpotentials and mass activities (normalized to Pt loadings) for PtCu NCs/C, Pt₄/C and commercial Pt/C catalysts. (c) HER polarization curves of Pt₄Cu/C and Pt₂Cu/C before and after 500 cycles at a rate of 10 mV/s.

PtCu NCs into acidic electrolyte would largely contribute to the changes in the concentration of metal active sites, and thus resulting in decreased mass activity of PtCu NCs/C catalysts. Surface overcoating with carbon nanoshells was further considered as a potential strategy for improving the stability of PtCu NCs/C towards the acidic HER catalysis.

3.2. Introduction of carbon nanoshell-overcoated PtCu NCs@C

3.2.1. Electrocatalyst characterizations

Carbon nanoshells, as structure-modification agents, can be introduced onto a catalyst surface through the subsequent decomposition and carbonization of organic composites at high temperatures [34,38]. As illustrated in Fig. 1, for one method of carbon nanoshell overcoating,

PVP and AA, the species initially involved for the colloidal synthesis of PtCu NCs, are directly introduced by the removal of solvent and are used as the precursors for carbon nanoshells after pyrolysis at 700 °C (method III-a). As an alternative method, PVP and AA are subsequently mixed with PtCu NCs/C based on a two-step protocol, followed by the final pyrolysis treatment (method III-b,c). Indeed, the latter synthesis pathway (i.e., method III-b,c) was more effective for the synthesis of PtCu NCs@C (vide infra). Structural characterizations including STEM and XAS together with the catalytic HER performance of PtCu-based catalysts prepared by method III-a are presented in the supporting information (Figs. S8, S9, S10, Table S1 and Table S2).

We attempted to probe the effect of the loadings of carbon nanoshells on electrocatalytic HER performance by adjusting the amount of PVP and AA organics on Pt₄Cu/C and Pt₂Cu/C. The resulting materials were denoted as PtCu@C-m-700, where “m” represents the loading of organics that are mixed with PtCu NCs/C prior to the pyrolysis treatment. ICP-OES analysis data for a set of PtCu@C-m-700 samples showed decreased loadings of Pt and Cu after overcoating with carbon nanoshells on the surface (Table S3). In the case of Pt₄Cu@C-100%-700, Pt loading was measured to be 11 wt%—nearly half the value (20 wt%) for Pt₄Cu/C prepared without the surface overcoating treatment. A carbonization yield of 30–32% for PVP and AA organics was estimated, which could be verified by TGA analysis on the mixture containing Pt₄Cu/C and 100% weight amount of organics, showing a 45% of weight loss when heated to 700 °C in a N₂ atmosphere (Fig. S11). The obtained TGA curve also suggested that the degradation process of organic PVP and AA mainly occurs in the temperature range from 120° to 500°C. The stage with a high rate of weight loss at 195–225 °C was related to the decomposition of AA compound [69]. Another stage was associated with the degradation of PVP polymer with the temperature (390 °C) slightly lower than that (400–530 °C) reported in the literature [70,71]. The process of metal particles sintering is generally favorable at high annealing temperatures (i.e., 700 °C) [72,73], so that the in situ introduction of carbon overlayers (occurs at below 600 °C, as indicated by TGA analysis) on the catalyst surface was expected, to some extent, to tackle metal particle sintering behavior on the PtCu-based materials.

STEM results show that PtCu NCs on Pt₄Cu/C and Pt₂Cu/C retain their averaged nanocrystal diameter after the annealing at 700 °C, regardless of the presence of carbon overlayers on the surface (Fig. 5). However, the overall morphology of PtCu nanostructures was evolved into solid large particles, which can be associated to the collapse and aggregation of small-sized PtCu NPs within the PtCu nanodendritic-like structures at high temperature [74]. PtCu NCs/C-700 and PtCu@C-m-700 with different loadings of carbon nanoshells were also investigated by measuring XRD, and the corresponding diffraction patterns are presented in Fig. 6a, b and Fig. S12. Compared to Pt₄Cu/C--derived samples, the diffraction peaks assigned to fcc structure of PtCu alloys of all the Pt₂Cu/C-derived samples appeared to be less distinct as a result of the smaller amount of metals that are loaded on the carbon support. The rhombohedral distortions revealed the additional diffraction peaks from Pt₂Cu/C-derived catalysts (Fig. S12). Similar distortions in a structure of PtCu intermetallics were observed before by Gong et al. [74] Refined rhombohedral phase (space group R-3 *m*) dominates over the fcc PtCu, but is less ordered than the latter. Around 60–75% of fcc phase was transformed into rhombohedral polymorph after the annealing treatment.

Fig. 6c shows that after annealing at 700 °C without the formation of carbon nanoshells on the surface, both Pt₄Cu/C-700 and Pt₂Cu/C-700 display an obviously increased particle size for the PtCu NCs, which is a consequence of the migration and coalescence of small-sized PtCu NPs [75]. For Pt₄Cu/C-derived catalysts, surface overcoating treatment can lead to a gradual increase in the refined particle size from 9.5 to 15 nm with increased carbon nanoshell loadings, while an opposite changing trend (from 10.5 to 4.8 nm, refined based on fcc structural model) was observed in the case of Pt₂Cu/C-derived samples. These results imply that the protective role of carbon overlayers in the suppression of

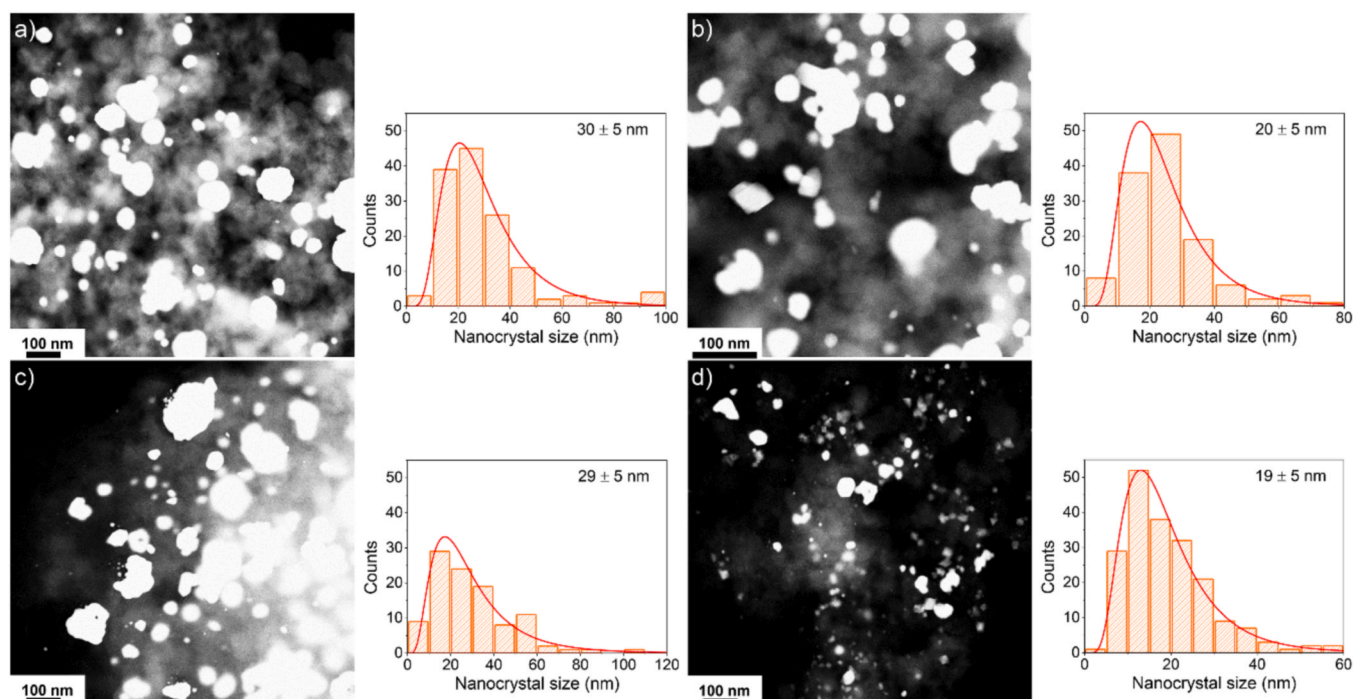


Fig. 5. STEM images of (a) Pt₄Cu/C-700, (b) Pt₄Cu@C-100%–700, (c) Pt₂Cu/C-700, (d) Pt₂Cu@C-100%–700. The size distributions for PtCu NCs are shown by following each image. Note that the images showed in (b) and (d) are belonging to the surface overcoated PtCu catalysts with carbon nanoshells.

particle sintering/agglomeration depends on the initial structure of PtCu NCs that are supported on the carbon material. In particular, in the case of Pt₄Cu/C, PtCu NCs consisting of a larger number of small-sized PtCu NPs with a close contact, are more prone to aggregate into large nanocrystals in the process of high-temperature pyrolysis [74]. The refined particle sizes for all the PtCu NCs@C nanomaterials are much smaller than the crystal sizes determined from STEM measurements, verifying again the nanoassembled structures of PtCu NCs, even after varying the degree of sintering in the presence of varied carbon nanoshell loadings on the surface.

Moreover, Pt lattice parameters decreased with increased loadings of carbon nanoshells (Fig. 6d), reflecting the lattice contraction of PtCu NCs on series of PtCu NCs@C catalysts [16]. Owing to a higher amount of Cu incorporated into Pt structure, the lattice contraction percentage (calculated with Equation S3 in the supporting information) for a set of Pt₂Cu@C-m-700 is about 2.9%, which is two times larger than what is observed for Pt₄Cu@C-m-700 samples (1.4%). In brief, the above results indicate that the atomic structure and nanocrystal size of the resulting PtCu NCs@C nanomaterials can be modified with a degree that depends on the carbon nanoshell loadings as well as the Cu atomic ratios of Pt₄Cu and Pt₂Cu NCs. Such structural characteristics of PtCu NCs@C nanomaterials are expected to bring out different catalytic features in terms of mass activity and long-term stability for the acidic HER.

3.2.2. HER performance of PtCu NCs@C

The effects of surface overcoating with carbon nanoshells on the electrochemical characteristics of different PtCu based catalysts were examined by collecting the CV curves in N₂-saturated 0.1 M HClO₄ electrolyte. The H_{upd} regions for Pt₄Cu/C-700 and Pt₂Cu/C-700, i.e., the samples annealed at 700 °C without surface overcoatings, decreased significantly as a consequence of the sintering of small-sized PtCu NPs at high temperatures (Fig. S13). PtCu NCs@C exhibited different CV curves, which can be originated from the carbon nanoshell loading dependency. With an increased loading of carbon nanoshells, the areas of H_{upd} region gradually increased for Pt₄Cu@C-m-700 prepared by the pyrolysis of Pt₄Cu/C with 30%, 60% amount of organics and Pt₂Cu@C-m-700 obtained through pyrolyzing 30%, 60% and 100% amount of

organics on Pt₂Cu/C (Fig. S13). Above results indicate that, once the carbon nanoshell loadings are not exceeded to be higher than 60% (for Pt₄Cu/C) or 100% (for Pt₂Cu/C), the catalytically active metal sites can be preserved through the protection by carbon overlayers, and in turn become accessible to the reactant and electrolyte. A further increase in carbon overlayer loadings could lead to a significantly lower capability of hydrogen sorption and subsequent lower reactivity of the catalyst such as Pt₄Cu@C-100%–700 and Pt₂Cu@C-200%–700, which serves as the consequence of the blockage of accessible metal active sites by the presence of carbon overlayers on surface. To further clarify the effect of surface carbon nanoshells, electric double-layer capacitance (C_{dl}) in the range of 0.26–0.46 V (vs. RHE) was measured with the scan rates of 5, 10, 20, 30, 40 mV/s (Fig. S14). It was observed that there is no clear correlation between the calculated C_{dl} values and the mass activities of HER for carbon nanoshell-overcoated and un-coated PtCu samples. This implies that not all the ions adsorption and desorption sites on the catalyst's surface are electrocatalytically active for the HER reaction [76]. The different C_{dl} values for carbon nanoshell-overcoated catalysts can be due to the loadings of carbon nanoshells and different amount of metal sites which are partially exposed on the surface. Obviously, the differences in the HER activities for the set of PtCu-based catalysts in this work are the consequence of changes in intrinsic activity, rather than metal loadings and surface area.

Fig. S15 shows the HER polarization curves and the overpotentials to deliver the geometrical current density of 10 mA/cm² for PtCu NCs/C, PtCu NCs/C-700 and carbon-overcoated PtCu NCs@C catalysts. Specifically, at the overpotential of 50 mV, the mass activity of HER on Pt₄Cu/C-700 dropped down by more than 93% comparing to that of Pt₄Cu/C, indicating a significant loss of active sites as a result of the metal nanoparticle sintering when treated at 700 °C. Surface overcoating with carbon nanoshells could render the HER activities of PtCu NCs@C differently enhanced. The analysis of the mass activity data of Pt₄Cu@C-m-700 materials demonstrated an increasing trend for Pt₄Cu@C-30%–700 and Pt₄Cu@C-60%–700, and then a slight drop for Pt₄Cu@C-100%–700 having the highest loading of carbon nanoshells (Fig. 7a). A mass activity of 1.64 A/mg_{Pt} at 100 mV of overpotential was further determined for Pt₄Cu@C-60%–700, which is more than six times

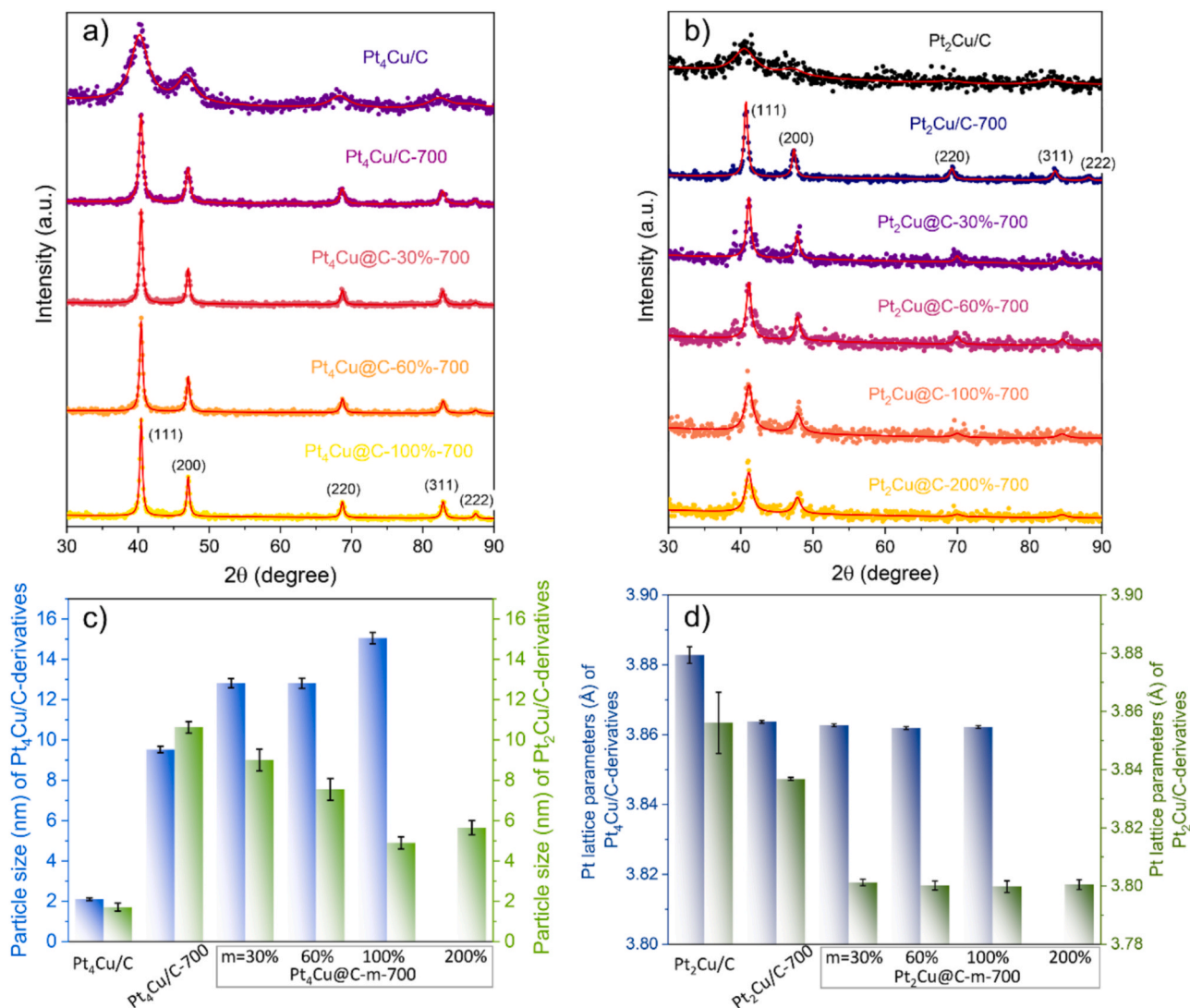


Fig. 6. The XRD patterns collected for (a) Pt₄Cu/C and its derivatives, (b) Pt₂Cu/C and its derivatives. The observed datasets were presented with dots, while the calculated model were marked with red lines (—). Refined particle size (c) and fcc-Pt lattice parameter (d) for these PtCu-based materials.

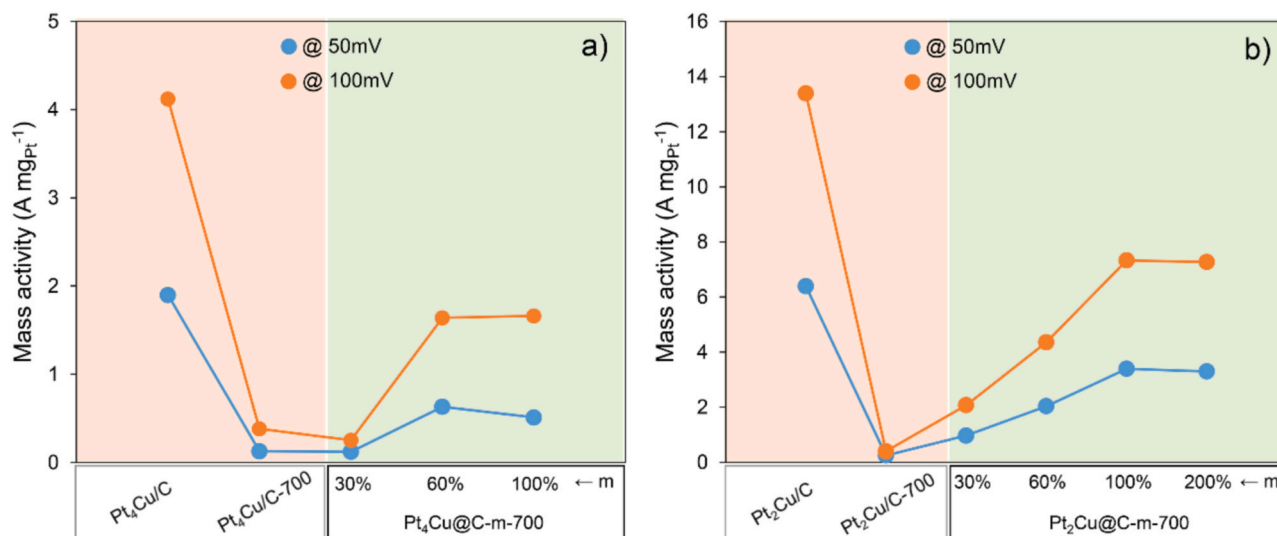


Fig. 7. The mass activity (normalized to Pt loading amount) at the potential of 50 and 100 mV for (a) Pt₄Cu/C, Pt₄Cu/C-700, Pt₄Cu@C-m-700 and (b) Pt₂Cu/C, Pt₂Cu/C-700 and Pt₂Cu@C-m-700. “m” represents the loading of organics that are mixed with PtCu NCs/C prior to pyrolysis.

higher than that ($0.25 \text{ A/mg}_{\text{Pt}}$) of $\text{Pt}_4\text{Cu@C-30\%-700}$. Interestingly, XRD results have indicated that $\text{Pt}_4\text{Cu@C-30\%-700}$ and $\text{Pt}_4\text{Cu@C-60\%-700}$ possess nearly the same refined particle sizes and Pt lattice parameters (Fig. 6c and d). This indicates that the variation in the HER catalytic activity is likely not a result of the differences in the exposed amount of metal active sites, when the existence of carbon nanoshells on the surface is not considered. Indeed, we suppose that the partial or incomplete overcoating of PtCu NCs with carbon overlayers accounts for the varied catalytic HER features. Further increasing carbon nanoshells loading, as exemplified by the $\text{Pt}_4\text{Cu@C-100\%-700}$ sample, can result in a larger particle size and higher extent of site-blockage, which in turn endows a markedly decreased accessibility of surface-active sites to reactant and electrolyte. Notably, the synergistic interactions between PtCu NPs and carbon nanoshells are also proposed to contribute to the higher mass activities of $\text{Pt}_4\text{Cu@C-m-700}$ than that observed for $\text{Pt}_4\text{Cu/C-700}$. Although the carbon nanoshells themselves are not active for the HER catalysis (Fig. S10), their presence on the surface can promote catalyst's conductivity and aids in controlling over the sorption properties of hydrogen intermediates on surface-active sites, thus manipulating the catalytic features of HER catalysis [77,78]. This hypothesis can be substantiated by the collected CV curves in Fig. S13, where the H_{upd} regions for $\text{Pt}_4\text{Cu/C-700}$ and $\text{Pt}_4\text{Cu@C-100\%-700}$ share the same areas, regardless of the difference in the refined particle size and the amount of exposed active sites on PtCu NCs.

The mass activities for $\text{Pt}_2\text{Cu@C-m-700}$ samples are compiled in

Fig. 7b, firstly showing a gradual increase of the values with varying organic loadings from 30% to 100% and then a slight decrease when changing the organic loading to 200%. In particular, at the overpotential of 100 mV, $\text{Pt}_2\text{Cu@C-100\%-700}$ exhibited a HER mass activity which is 18 times higher than that of $\text{Pt}_2\text{Cu/C-700}$ without surface overcoatings. In contrast to the case of $\text{Pt}_4\text{Cu@C-m-700}$, the protective role of carbon nanoshells in suppression of metal nanoparticle sintering on $\text{Pt}_2\text{Cu@C-m-700}$ has been reliably identified by the measured XRD patterns (Fig. 6). That is, surface overcoating with carbon nanoshells is an effective strategy of preventing the sintering of Pt_2Cu NCs, the latter have been characterized by STEM imaging to be rather loosely packed nanodendrites or nanoassemblies (Fig. 2f). The obvious enhancements in the HER mass activity for $\text{Pt}_2\text{Cu@C-m-700}$, compared to that of $\text{Pt}_2\text{Cu/C-700}$, are a consequence of the well preserved active sites (i.e., less sintering of PtCu NCs with smaller nanocrystal sizes) and the synergistic effect from carbon nanoshells on the surface [77,78]. It should be emphasized that all the carbon-overcoated PtCu NCs@C nanomaterials possess lower HER mass activities in comparison with PtCu NCs/C, the samples synthesized by the wet-chemical method and without overcoatings on the surface (Fig. 7).

The long-term stability of $\text{Pt}_4\text{Cu@C-60\%-700}$, $\text{Pt}_4\text{Cu@C-100\%-700}$, $\text{Pt}_2\text{Cu@C-60\%-700}$, $\text{Pt}_2\text{Cu@C-100\%-700}$ was measured by collecting the corresponding HER polarization curves after continuous 500 cycles. As summarized in Fig. 8, unexpectedly decreased HER mass activities at the overpotential of 50 mV were determined after the

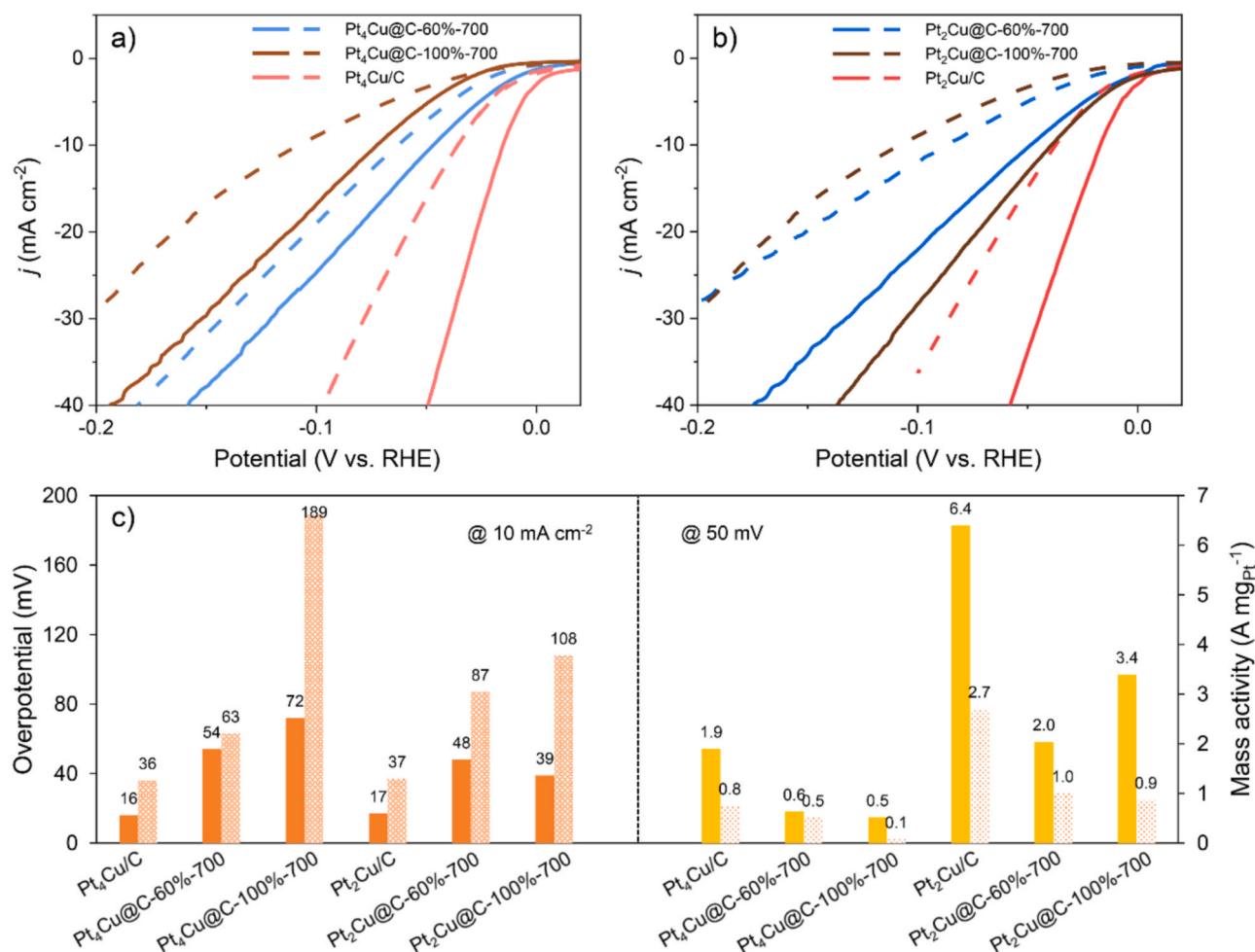


Fig. 8. (a, b) HER polarization curves, (c) overpotential and mass activity (normalized to Pt loading amount, at 50 mV) for $\text{Pt}_4\text{Cu/C}$, $\text{Pt}_4\text{Cu@C-60\%-700}$, $\text{Pt}_4\text{Cu@C-100\%-700}$, $\text{Pt}_2\text{Cu/C}$, $\text{Pt}_2\text{Cu@C-60\%-700}$, $\text{Pt}_2\text{Cu@C-100\%-700}$ before and after 500 cycles at a rate of 10 mV/s. Solid and dashed lines in (a, b) represent the HER polarization curves collected before and after 500 cycles, respectively. The initial values of overpotential and mass activity in (c) are shown with solid-filled columns, while those after 500 cycles are drawn with pattern-filled columns.

durability tests. To be more specific, as low as 16.7% loss of mass activity was determined for Pt₄Cu@C-60%–700, the catalyst showing the mass activity three times lower than the Pt₄Cu/C sample without overcoatings. The activity-stability trade-off relationship clearly hold true for above two samples. In contrast, Pt₄Cu@C-100%–700 delivered the worst mass activity (0.1 A/mg_{Pt}) after the durability test, which was 80% dropped in comparison with its beginning-of-the-life activity (0.5 A/mg_{Pt}). Chemical stability test results already showed an obviously decreased amount of Cu leached from Pt₄Cu@C-100%–700 (Fig. S7). This is due to the positive role of carbon nanoshells; surface overcoatings could function as a physical barrier to prevent the accessibility of protons or poisonous substance to the internal metal sites [79]. The only fewer PtCu active sites that are not covered after surface overcoating treatment on Pt₄Cu@C-100%–700 would probably undergo an irreversible dissolution process during the potential cycling, which makes the active sites present at the electrode surface to be insufficient to trigger the HER catalysis. Note that the mass activity of Pt₄Cu/C after the durability test is still much higher than the beginning-of-the-life activity of both Pt₄Cu@C-60%–700 and Pt₄Cu@C-100%–700. Such activity drops are mainly because of the active sites loss through the blockage by carbon overlayers and the sintering of PtCu NPs within each PtCu nanodendrite in the process of surface overcoating treatment.

In addition, the HER mass activity loss for Pt₂Cu@C-60%–700 under the same condition was around 50%, which is comparable with that (58%) of un-coated Pt₂Cu/C sample. Pt₂Cu@C-100%–700, the most active one among the carbon nanoshell-coated Pt₂Cu@C-m-700, exhibited more than 73% loss of its mass activity towards the acidic HER after 500 cycles. Carbon nanoshells tend to play a minor role in protecting Cu atoms from dissolution, as observed from the chemical stability tests (Fig. S7). In addition, the collected STEM images of Pt₂Cu@C-100%–700 have suggested an unchanged morphology of PtCu NCs on carbon support after the electrochemical stability test (Fig. S16). These results indicate that mass activity loss for Pt₂Cu@C-100%–700 is mainly the consequence of the dissolution of Cu atoms from PtCu NPs (averaged 5 nm in diameter, Fig. 6). A decreased amount of Cu being alloyed with Pt on catalyst surface would result in a modified electronic structure of active sites, thereby displaying a reduced activity towards the acidic HER. This can be used to explain the activity drops for other Pt₂Cu@C-m-700 samples. Comparisons of the HER performance of Pt₂Cu/C and Pt₂Cu@C-60%–700 as well as Pt₂Cu@C-100%–700 suggest that the Pt₂Cu/C sample stands out to manifest both high activity and long-term durability for the HER catalysis. These results imply the limitations of surface overcoating of PtCu nanostructures with carbon nanoshells for high-performing electrocatalysts with the applications in acidic HER. That is, the opposite trends observed for the particle size evolution of Pt₄Cu and Pt₂Cu NCs during the annealing, and the obvious loss of catalytic activity as well as the limited gains in catalytic/structural stability question the versatility of surface overcoating engineering. Advanced synthetic strategies, not limited to the surface overcoating engineering, for the design and optimization of high-performance metal-based alloy nanocatalysts and bi-functional electrocatalysts (e.g., for water splitting reactions) with both high activity and long-term durability are thus highly desirable [77,78,80–82].

4. Conclusions

Through tailoring the atomic compositions and deploying surface overcoating engineering, a series of PtCu-based catalysts were synthesized in this work to hold the merits as followings: (i) nanoporous and nanodendritic structure of PtCu nanocrystals (NCs); (ii) electronic interactions on PtCu-alloyed nanostructures; (iii) surface encapsulation of PtCu NCs with varied amount of porous carbon nanoshells. The rationally tailored structural features of carbon-supported PtCu NCs have been characterized by performing catalytic performance tests on the acidic hydrogen evolution reaction (HER). Results indicate that alloying

of Pt with Cu could achieve a HER mass activity that is several times higher than that of the commercial Pt/C counterpart as well as a relatively good stability in the acidic electrolyte. It was also revealed that the combination of carbon overcoatings with the rationally designed PtCu NCs by forming a distinct nanostructure endows the noble-metal-based nanocatalyst with decreased active site accessibility, impacting reactant sorption and surface catalysis. The degree of synergy effect between exposed active sites and carbon overlayers depends on the initial structure of PtCu nanodendrites and carbon overcoating loadings on the surface, thereby varying the influences on their intrinsic reactivity of acidic HER. This work demonstrates the challenge of breaking the activity-stability trade-off relations by performing surface engineering on carbon-supported PtCu nanodendritic-like nanostructures, questioning the commonly accepted benefits from overcoating of Pt or Pt-based alloyed nanoparticles for high-performance electrocatalysis. Such findings further suggest the necessity for investigating the influence of overcoatings (e.g., carbon nanoshells) on the catalytic performance of other kinds of transition metal-based nanostructures when employed for important electrochemical transformations.

CRediT authorship contribution statement

Qiang Liu: Formal analysis, Investigation, Methodology, Visualization, Writing – original draft, Writing – review and editing. **Joseph Tripp:** Formal analysis, Investigation, Writing – review and editing. **Claire Mitchell:** Formal analysis, Investigation, Writing – review and editing. **Przemyslaw Rzepka:** Formal analysis, Writing – review and editing. **Ilia I. Sadykov:** Formal analysis, Investigation, Methodology, Writing – review and editing. **Arik Beck:** Investigation, Methodology, Writing – review and editing. **Frank Krumeich:** Investigation, Methodology, Writing – review and editing. **Srijita Nundy:** Investigation, Writing – review and editing. **Luca Artiglia:** Formal analysis, Methodology, Writing – review and editing. **Marco Ranocchiari:** Resources, Writing – review and editing. **Jeroen A. van Bokhoven:** Supervision, Resources, Project administration, Funding acquisition, Writing – review and editing.

Declaration of Competing Interest

The authors declare that they have no known competing financial interests or personal relationships that could have appeared to influence the work reported in this paper.

Data availability

Data will be made available on request.

Acknowledgements

This work has received funding from the European Union's Horizon 2020 research and innovation program under grant agreement No 875524. The authors thank Scientific Center for Optical and Electron Microscopy (ScopeM) at ETH Zurich, X-ray photoelectron spectroscopy beamline and SuperXAS beamline at Swiss Light Source (SLS) for the measurement assistance and technical support. They are also grateful to Dr. Kamuran Yasadi (Elestor, the Netherlands), Dr. Vignesh Balasubramanian (Elestor, the Netherlands) and Dr. Peter Klusener (Shell, the Netherlands) for fruitful discussions and valuable comments.

Notes

The content of this publication does not reflect the official opinion of the European Union. Responsibility for the information in this report lies entirely with the authors.

Appendix A. Supporting information

Supplementary data associated with this article can be found in the online version at [doi:10.1016/j.jallcom.2023.172128](https://doi.org/10.1016/j.jallcom.2023.172128).

References

- [1] C. Bhowmik, S. Bhowmik, A. Ray, K.M. Pandey, Optimal green energy planning for sustainable development: a review, *Renew. Sustain. Energy Rev.* 71 (2017) 796–813, <https://doi.org/10.1016/j.rser.2016.12.105>.
- [2] J.A. Turner, Sustainable hydrogen production, *Science* 305 (2004) 972–974, <https://doi.org/10.1126/science.1103197>.
- [3] J.A. Turner, A realizable renewable energy future, *Science* 285 (1999) 687–689, <https://doi.org/10.1126/science.285.5428.687>.
- [4] J. Zhu, L. Hu, P. Zhao, L.Y.S. Lee, K.-Y. Wong, Recent advances in electrocatalytic hydrogen evolution using nanoparticle catalysts, *Chem. Rev.* 120 (2020) 851–918, <https://doi.org/10.1021/acs.chemrev.9b00248>.
- [5] K.T. Cho, P. Ridgway, A.Z. Weber, S. Haussener, V. Battaglia, V. Srinivasan, High performance hydrogen/bromine redox flow battery for grid-scale energy storage, *J. Electrochem. Soc.* 159 (2012) A1806, <https://doi.org/10.1149/2.018211jes>.
- [6] H. Kreutzer, V. Yarglagadda, T.V. Nguyen, Performance evaluation of a regenerative hydrogen-bromine fuel cell, *J. Electrochem. Soc.* 159 (2012) F331, <https://doi.org/10.1149/2.086207jes>.
- [7] W. Sheng, M. Myint, J.G. Chen, Y. Yan, Correlating the hydrogen evolution reaction activity in alkaline electrolytes with the hydrogen binding energy on monometallic surfaces, *Energy Environ. Sci.* 6 (2013) 1509–1512, <https://doi.org/10.1039/C3EE00045A>.
- [8] S.R. Challa, A.T. Delariva, T.W. Hansen, S. Helveg, J. Sehested, P.L. Hansen, F. Garzon, A.K. Datye, Relating rates of catalyst sintering to the disappearance of individual nanoparticles during Ostwald ripening, *J. Am. Chem. Soc.* 133 (2011) 20672–20675, <https://doi.org/10.1021/ja208324n>.
- [9] J.C. Meier, C. Galeano, I. Katsounaros, J. Witte, H.J. Bongard, A.A. Topalov, C. Baldizzone, S. Mezzavilla, F. Schüth, K.J.J. Mayrhofer, Design criteria for stable Pt/C fuel cell catalysts, *Beilstein J. Nanotechnol.* 5 (2014) 44–67, <https://doi.org/10.3762/bjnano.5.5>.
- [10] X. Zou, Y. Zhang, Noble metal-free hydrogen evolution catalysts for water splitting, *Chem. Soc. Rev.* 44 (2015) 5148–5180, <https://doi.org/10.1039/C4CS00448E>.
- [11] P.P. Lopes, D. Li, H. Lv, C. Wang, D. Tripkovic, Y. Zhu, R. Schimmenti, H. Daimon, Y. Kang, J. Snyder, N. Becknell, K.L. More, D. Strmcnik, N.M. Markovic, M. Mavrikakis, V.R. Stamenkovic, Eliminating dissolution of platinum-based electrocatalysts at the atomic scale, *Nat. Mater.* 19 (2020) 1207–1214, <https://doi.org/10.1038/s41563-020-0735-3>.
- [12] Z. Liu, J. Qi, M. Liu, S. Zhang, Q. Fan, H. Liu, K. Liu, H. Zheng, Y. Yin, C. Gao, Aqueous synthesis of ultrathin platinum/non-noble metal alloy nanowires for enhanced hydrogen evolution activity, *Angew. Chem. Int. Ed.* 57 (2018) 11678–11682, <https://doi.org/10.1002/anie.201806194>.
- [13] L. Li, S. Wang, L. Xiong, B. Wang, G. Yang, S. Yang, Surface-engineered mesoporous Pt nanodendrites with Ni dopant for highly enhanced catalytic performance in hydrogen evolution reaction, *J. Mater. Chem. A* 7 (2019) 12800–12807, <https://doi.org/10.1039/C9TA02696G>.
- [14] Z. Xia, S. Guo, Strain engineering of metal-based nanomaterials for energy electrocatalysis, *Chem. Soc. Rev.* 48 (2019) 3265–3278, <https://doi.org/10.1039/C8CS00846A>.
- [15] J.R. Kitchin, J.K. Nørskov, M.A. Barteau, J.G. Chen, Role of strain and ligand effects in the modification of the electronic and chemical properties of bimetallic surfaces, *Phys. Rev. Lett.* 93 (2004), 156801, <https://doi.org/10.1103/PhysRevLett.93.156801>.
- [16] Y. Zhao, Y. Wu, J. Liu, F. Wang, Dependent relationship between quantitative lattice contraction and enhanced oxygen reduction activity over Pt–Cu alloy catalysts, *ACS Appl. Mater. Interfaces* 9 (2017) 35740–35748, <https://doi.org/10.1021/acsami.7b08437>.
- [17] V.R. Stamenkovic, B.S. Mun, M. Arenz, K.J.J. Mayrhofer, C.A. Lucas, G. Wang, P. N. Ross, N.M. Markovic, Trends in electrocatalysis on extended and nanoscale Pt-bimetallic alloy surfaces, *Nat. Mater.* 6 (2007) 241–247, <https://doi.org/10.1038/nmat1840>.
- [18] H.-J. Qiu, H.T. Xu, X. Li, J.Q. Wang, Y. Wang, Core-shell-structured nanoporous PtCu with high Cu content and enhanced catalytic performance, *J. Mater. Chem. A* 3 (2015) 7939–7944, <https://doi.org/10.1039/C5TA00020C>.
- [19] J. Wang, J.W. Chen, J.D. Chen, H. Zhu, M. Zhang, M.L. Du, Designed synthesis of size-controlled Pt-Cu alloy nanoparticles encapsulated in carbon nanofibers and their high efficient electrocatalytic activity toward hydrogen evolution reaction, *Adv. Mater. Interfaces* 4 (2017), 1700005, <https://doi.org/10.1002/admi.201700005>.
- [20] W. Li, Z.-Y. Hu, Z. Zhang, P. Wei, J. Zhang, Z. Pu, J. Zhu, D. He, S. Mu, G. V. Tendeloo, Nano-single crystal coalesced PtCu nanospheres as robust bifunctional catalyst for hydrogen evolution and oxygen reduction reactions, *J. Catal.* 375 (2019) 164–170, <https://doi.org/10.1016/j.jcat.2019.05.031>.
- [21] H. Guo, X. Liu, C. Bai, Y. Chen, L. Wang, M. Zheng, Q. Dong, D.-L. Peng, Effect of component distribution and nanoporosity in CuPt nanotubes on electrocatalysis of the oxygen reduction reaction, *ChemSusChem* 8 (2015) 486–494, <https://doi.org/10.1002/cssc.201403037>.
- [22] H.-H. Li, Q.-Q. Fu, L. Xu, S.-Y. Ma, Y.-R. Zheng, X.-J. Liu, S.-H. Yu, Highly crystalline PtCu nanotubes with three dimensional molecular accessible and restructured surface for efficient catalysis, *Energy Environ. Sci.* 10 (2017) 1751–1756, <https://doi.org/10.1039/C7EE00573C>.
- [23] B.Y. Xia, H.B. Wu, X. Wang, X.W. Lou, One-pot synthesis of cubic PtCu₃ nanocages with enhanced electrocatalytic activity for the methanol oxidation reaction, *J. Am. Chem. Soc.* 134 (2012) 13934–13937, <https://doi.org/10.1021/ja3051662>.
- [24] S. Chen, H. Su, Y. Wang, W. Wu, J. Zeng, Size-controlled synthesis of platinum–copper hierarchical trigonal bipyramid nanoframes, *Angew. Chem. Int. Ed.* 54 (2015) 108–113, <https://doi.org/10.1002/anie.201408399>.
- [25] X.-F. Zhang, A.-J. Wang, L. Zhang, J. Yuan, Z. Li, J.-J. Feng, Solvothermal synthesis of platinum–copper dodecahedral nanoframes with enhanced catalytic activity and durability for hydrogen evolution reaction, *ACS Appl. Energy Mater.* 1 (2018) 5054–5061, <https://doi.org/10.1021/acsaem.8b01065>.
- [26] H.-J. Niu, H.-Y. Chen, G.-L. Wen, J.-J. Feng, Q.-L. Zhang, A.-J. Wang, One-pot solvothermal synthesis of three-dimensional hollow PtCu alloyed dodecahedron nanoframes with excellent electrocatalytic performances for hydrogen evolution and oxygen reduction, *J. Colloid Interface Sci.* 539 (2019) 525–532, <https://doi.org/10.1016/j.jcis.2018.12.066>.
- [27] L. Guo, L.-B. Huang, W.-J. Jiang, Z.-D. Wei, L.-J. Wan, J.-S. Hu, Tuning the branches and composition of PtCu nanodendrites through underpotential deposition of Cu towards advanced electrocatalytic activity, *J. Mater. Chem. A* 5 (2017) 9014–9021, <https://doi.org/10.1039/C7TA01859B>.
- [28] Y. Du, K. Ni, Q. Zhai, Y. Yun, Y. Xu, H. Sheng, Y. Zhu, M. Zhu, Facile air oxidative induced dealloying of hierarchical branched PtCu nanodendrites with enhanced activity for hydrogen evolution, *Appl. Catal. A* 557 (2018) 72–78, <https://doi.org/10.1016/j.apcata.2018.03.014>.
- [29] Q. Liu, M. Ranocchiari, J.A. van Bokhoven, Catalyst overcoating engineering towards high-performance electrocatalysis, *Chem. Soc. Rev.* 51 (2022) 188–236, <https://doi.org/10.1039/D1CS00270H>.
- [30] S. Chen, Z. Wei, X. Qi, L. Dong, Y.-G. Guo, L. Wan, Z. Shao, L. Li, Nanostructured polyaniline-decorated Pt/C@PANI core-shell catalyst with enhanced durability and activity, *J. Am. Chem. Soc.* 134 (2012) 13252–13255, <https://doi.org/10.1021/ja306501x>.
- [31] A.-L. Wang, H. Xu, J.-X. Feng, L.-X. Ding, Y.-X. Tong, G.-R. Li, Design of Pd/PANI/Pd sandwich-structured nanotube array catalysts with special shape effects and synergistic effects for ethanol electrooxidation, *J. Am. Chem. Soc.* 135 (2013) 10703–10709, <https://doi.org/10.1021/ja403101r>.
- [32] G. Gershinsky, P. Nanikashvili, R. Elazari, D. Zitoun, From the sea to hydrobromic acid: polydopamine layer as corrosion protective layer on platinum electrocatalyst, *ACS Appl. Energy Mater.* 1 (2018) 4678–4685, <https://doi.org/10.1021/acsaem.8b00808>.
- [33] K. Cheng, Z. Kou, J. Zhang, M. Jiang, H. Wu, L. Hu, X. Yang, M. Pana, S. Mu, Ultrathin carbon layer stabilized metal catalysts towards oxygen reduction, *J. Mater. Chem. A* 3 (2015) 14007–14014, <https://doi.org/10.1039/C5TA02386F>.
- [34] D.Y. Chung, S.W. Jun, G. Yoon, S.G. Kwon, D.Y. Shin, P. Seo, J.M. Yoo, H. Shin, Y.-H. Chung, H. Kim, B.S. Mun, K.-S. Lee, N.-S. Lee, S.J. Yoo, D.-H. Lim, K. Kang, Y.-E. Sung, T. Hyeon, Highly durable and active PtFe nanocatalyst for electrochemical oxygen reduction reaction, *J. Am. Chem. Soc.* 137 (2015) 15478–15485, <https://doi.org/10.1021/jacs.5b09653>.
- [35] S. Takenaka, A. Hirata, E. Tanabe, H. Matsune, M. Kishida, Preparation of supported Pt–Co alloy nanoparticle catalysts for the oxygen reduction reaction by coverage with silica, *J. Catal.* 274 (2010) 228–238, <https://doi.org/10.1016/j.jcat.2010.07.005>.
- [36] S. Kang, F. Xia, Z. Hu, W. Hu, Y. She, L. Wang, X. Fu, W. Lu, Platinum nanoparticles with TiO₂-skin as a durable catalyst for photoelectrochemical methanol oxidation and electrochemical oxygen reduction reactions, *Electrochim. Acta* 343 (2020), 136119, <https://doi.org/10.1016/j.electacta.2020.136119>.
- [37] L. Guo, W.-J. Jiang, Y. Zhang, J.-S. Hu, Z.-D. Wei, L.-J. Wan, Embedding Pt nanocrystals in N-doped porous carbon/carbon nanotubes toward highly stable electrocatalysts for the oxygen reduction reaction, *ACS Catal.* 5 (2015) 2903–2909, <https://doi.org/10.1021/acscatal.5b00117>.
- [38] M. Karuppannan, Y. Kim, S. Gok, E. Lee, J.Y. Hwang, J.-H. Jang, Y.-H. Cho, T. Lim, Y.-E. Sung, O.J. Kwon, A highly durable carbon-nanofiber-supported Pt-C core-shell cathode catalyst for ultra-low Pt loading proton exchange membrane fuel cells: facile carbon encapsulation, *Energy Environ. Sci.* 12 (2019) 2820–2829, <https://doi.org/10.1039/C9EE01000A>.
- [39] S. Li, R. Wang, X. Yang, J. Wu, H. Meng, H. Xu, Z. Ren, Binary metal phosphides with MoP and FeP embedded in P,N-doped graphitic carbon as electrocatalysts for oxygen reduction, *ACS Sustain. Chem. Eng.* 7 (2019) 11872–11884, <https://doi.org/10.1021/acssuschemeng.9b02473>.
- [40] S. Huang, Y. Meng, S. He, A. Goswami, Q. Wu, J. Li, S. Tong, T. Asefa, M. Wu, N.-O., and S-tridoped carbon-encapsulated Co₉S₈ nanomaterials: efficient bifunctional electrocatalysts for overall water splitting, *Adv. Func. Mater.* 27 (2017), 1606585, <https://doi.org/10.1002/adfm.201606585>.
- [41] Z. Shi, Y. Wang, H. Lin, H. Zhang, M. Shen, S. Xie, Y. Zhang, Q. Gao, Y. Tang, Porous nanoMoC@graphite shell derived from a MOFs-directed strategy: an efficient electrocatalyst for the hydrogen evolution reaction, *J. Mater. Chem. A* 4 (2016) 6006–6013, <https://doi.org/10.1039/C6TA01900E>.
- [42] Z. Wang, B. Li, X. Ge, F.W.T. Goh, X. Zhang, G. Du, D. Wu, Z. Liu, T.S.A. Hor, H. Zhang, Y. Zong, Co@Co₃O₄@PPD core@bimetallic nanoparticle-based composite as an efficient electrocatalyst for oxygen reduction reaction, *Small* 12 (2016) 2580–2587, <https://doi.org/10.1002/sml.201503694>.
- [43] X. Cui, P. Ren, D. Deng, J. Deng, X. Bao, Single layer graphene encapsulating non-precious metals as high-performance electrocatalysts for water oxidation, *Energy Environ. Sci.* 9 (2016) 123–129, <https://doi.org/10.1039/C5EE03316K>.

- [44] Z. Kou, K. Cheng, H. Wu, R. Sun, B. Guo, S. Mu, Observable electrochemical oxidation of carbon promoted by platinum nanoparticles, *ACS Appl. Mater. Interfaces* 8 (2016) 3940–3947, <https://doi.org/10.1021/acsami.5b11086>.
- [45] K. Eid, H. Wang, P. He, K. Wang, T. Ahmad, S.M. Alshehri, Y. Yamauchi, L. Wang, One-step synthesis of porous bimetallic PtCu nanocrystals with high electrocatalytic activity for methanol oxidation reaction, *Nanoscale* 7 (2015) 16860–16866, <https://doi.org/10.1039/C5NR04557F>.
- [46] Z. Zhang, Z. Luo, B. Chen, C. Wei, J. Zhao, J. Chen, X. Zhang, Z. Lai, Z. Fan, C. Tan, M. Zhao, Q. Lu, B. Li, Y. Zong, C. Yan, G. Wang, Z.J. Xu, H. Zhang, One-pot synthesis of highly anisotropic five-fold-twinned PtCu nanoframes used as a bifunctional electrocatalyst for oxygen reduction and methanol oxidation, *Adv. Mater.* 28 (2016) 8712–8717, <https://doi.org/10.1002/adma.201603075>.
- [47] M. Gong, G. Fu, Y. Chen, Y. Tang, T. Lu, Autocatalysis and selective oxidative etching induced synthesis of platinum–copper bimetallic alloy nanodendrites electrocatalysts, *ACS Appl. Mater. Interfaces* 6 (2014) 7301–7308, <https://doi.org/10.1021/am500656j>.
- [48] L. Zhang, J. Zhang, Q. Kuang, S. Xie, Z. Jiang, Z. Xie, L. Zheng, Cu²⁺-assisted synthesis of hexoctahedral Au–Pd alloy nanocrystals with high-index facets, *J. Am. Chem. Soc.* 133 (2011) 17114–17117, <https://doi.org/10.1021/ja2063617>.
- [49] Y. Jiang, Y. Jia, J. Zhang, L. Zhang, H. Huang, Z. Xie, L. Zheng, Underpotential deposition-induced synthesis of composition-tunable Pt–Cu nanocrystals and their catalytic properties, *Chem. A Eur. J.* 19 (2013) 3119–3124, <https://doi.org/10.1002/chem.201203729>.
- [50] N.V. Long, M. Ohtaki, M. Nogami, T.D. Hien, Effects of heat treatment and poly(vinylpyrrolidone) (PVP) polymer on electrocatalytic activity of polyhedral Pt nanoparticles towards their methanol oxidation, *Colloid Polym. Sci.* 289 (2011) 1373–1386, <https://doi.org/10.1007/s00396-011-2460-6>.
- [51] K. Eid, Y.H. Ahmad, H. Yu, Y. Li, X. Li, S.Y. AlQaradawi, H. Wang, L. Wang, Rational one-step synthesis of porous PtPdRu nanodendrites for ethanol oxidation reaction with a superior tolerance for CO-poisoning, *Nanoscale* 9 (2017) 18881–18889, <https://doi.org/10.1039/C7NR07609F>.
- [52] J. Wang, X.-B. Zhang, Z.-L. Wang, L.-M. Wang, W. Xing, X. Liu, One-step and rapid synthesis of “clean” and monodisperse dendritic Pt nanoparticles and their high performance toward methanol oxidation and p-nitrophenol reduction, *Nanoscale* 4 (2012) 1549–1552, <https://doi.org/10.1039/C2NR11912A>.
- [53] V. Petkov, Y. Maswadeh, J.A. Vargas, S. Shan, H. Kareem, Z.-P. Wu, J. Luo, C.-J. Zhong, S. Shastri, P. Kenesei, Deviations from Vegard’s law and evolution of the electrocatalytic activity and stability of Pt-based nanoalloys inside fuel cells by *in operando* X-ray spectroscopy and total scattering, *Nanoscale* 11 (2019) 5512–5525, <https://doi.org/10.1039/C9NR01069F>.
- [54] N. Tsubouchi, C. Xu, Y. Ohtsuka, Carbon crystallization during high-temperature pyrolysis of coals and the enhancement by calcium, *Energy Fuels* 17 (2003) 1119–1125, <https://doi.org/10.1021/ef020265u>.
- [55] P. Mani, R. Srivastava, P. Strasser, Dealloyed Pt–Cu core–shell nanoparticle electrocatalysts for use in PEM fuel cell cathodes, *J. Phys. Chem. C* 112 (2008) 2770–2778, <https://doi.org/10.1021/jp0776412>.
- [56] X. Li, X. Wang, I.I. Sadykov, D. Palagin, O.V. Safonova, J. Li, A. Beck, F. Krumeich, J.A. van Bokhoven, L. Artiglia, Temperature and reaction environment influence the nature of platinum species supported on ceria, *ACS Catal.* 11 (2021) 13041–13049, <https://doi.org/10.1021/acscatal.1c03165>.
- [57] C.D. Wanger, W.M. Riggs, L.E. Davis, J.F. Moulder, G.E. Muilenberg, *Handbook of X-ray photo-electron spectroscopy*. Perkin-Elmer Corporation, Physical Electronics Division, Eden Prairie, Minnesota, USA 1979.
- [58] L. Qiu, F. Liu, L. Zhao, W. Yang, J. Yao, Evidence of a unique electron donor-acceptor property for platinum nanoparticles as studied by XPS, *Langmuir* 22 (2006) 4480–4482, <https://doi.org/10.1021/la053071q>.
- [59] J. Liu, G. Xu, B. Liu, J. Zhang, A dendritic core–shell Cu@PtCu alloy electrocatalyst resulting in an enhanced electron transfer ability and boosted surface active sites for an improved methanol oxidation reaction, *Chem. Commun.* 53 (2017) 7457–7460, <https://doi.org/10.1039/C7CC01559C>.
- [60] Z. Sun, J. Masa, W. Xia, D. König, A. Ludwig, Z.-A. Li, M. Farle, W. Schuhmann, M. Muhler, Rapid and surfactant-free synthesis of bimetallic Pt–Cu nanoparticles simply via ultrasound-assisted redox replacement, *ACS Catal.* 2 (2012) 1647–1653, <https://doi.org/10.1021/cs300187z>.
- [61] X. Peng, D. Chen, X. Yang, D. Wang, M. Li, C.-C. Tseng, R. Panneerselvam, X. Wang, W. Hu, J. Tian, Y. Zhao, Microwave-assisted synthesis of highly dispersed PtCu nanoparticles on three-dimensional nitrogen-doped graphene networks with remarkably enhanced methanol electrooxidation, *ACS Appl. Mater. Interfaces* 8 (2016) 33673–33680, <https://doi.org/10.1021/acsami.6b11800>.
- [62] J. Huang, Y. Song, D. Ma, Y. Zheng, M. Chen, H. Wan, The effect of the support on the surface composition of PtCu alloy nanocatalysts: in situ XPS and HS-LEIS studies, *Chin. J. Catal.* 38 (2017) 1229–1236, [https://doi.org/10.1016/S1872-2067\(17\)62857-2](https://doi.org/10.1016/S1872-2067(17)62857-2).
- [63] S. Wang, T. Kou, J.B. Varley, S.A. Akhade, S.E. Weitzner, S.E. Baker, E.B. Duoss, Y. Li, Cu₂O/CuS nanocomposites show excellent selectivity and stability for formate generation via electrochemical reduction of carbon dioxide, *ACS Mater. Lett.* 3 (2021) 100–109, <https://doi.org/10.1021/acsmaterlett.0c00520>.
- [64] C. Zhang, P. Wang, W. Li, Z. Zhang, J. Zhu, Z. Pu, Y. Zhao, S. Mu, MOF-assisted synthesis of octahedral carbon-supported PtCu nanoalloy catalysts for an efficient hydrogen evolution reaction, *J. Mater. Chem. A* 8 (2020) 19348–19356, <https://doi.org/10.1039/D0TA06632J>.
- [65] S. Henning, L. Kühn, J. Herranz, M. Nachtegaal, R. Hübner, M. Werheid, A. Eychmüller, T.J. Schmidt, Effect of acid washing on the oxygen reduction reaction activity of Pt–Cu aerogel catalysts, *Electrochim. Acta* 233 (2017) 210–217, <https://doi.org/10.1016/j.electacta.2017.03.019>.
- [66] S. Anantharaj, S. Noda, M. Driess, P.W. Menezes, The pitfalls of using potentiodynamic polarization curves for Tafel analysis in electrocatalytic water splitting, *ACS Energy Lett.* 6 (2021) 1607–1611, <https://doi.org/10.1021/acsenenergyl.1c00608>.
- [67] J.O.’M. Bockris, T. Otagawa, Mechanism of oxygen evolution on perovskites, *J. Phys. Chem.* 87 (1983) 2960–2971, <https://doi.org/10.1021/j100238a048>.
- [68] G. Fu, H. Liu, N. You, J. Wu, D. Sun, L. Xu, Y. Tang, Y. Chen, Dendritic platinum–copper bimetallic nanoassemblies with tunable composition and structure: Arginine-driven self-assembly and enhanced electrocatalytic activity, *Nano Res.* 9 (2016) 755–765, <https://doi.org/10.1007/s12274-015-0954-0>.
- [69] A. Pielasz, A. Gawlowski, J. Fabia, C. Ślusarczyk, E. Sarna, Inhibitors of thermally induced burn incidents—the examinations of the flammability, TGA, SAXS and SEM methods, *Polymer* 62 (2017) 806–811, <https://doi.org/10.14314/polimery.2017.806>.
- [70] G. Bianco, M.S. Soldi, E.A. Pinheiro, A.T.N. Pires, M.H. Gehlen, V. Soldi, Thermal stability of poly(N-vinyl-2-pyrrolidone-co-methacrylic acid) copolymers in inert atmosphere, *Polym. Degrad. Stab.* 80 (2003) 567–574, [https://doi.org/10.1016/S0141-3910\(03\)00053-3](https://doi.org/10.1016/S0141-3910(03)00053-3).
- [71] M.H. Abou Taleb, Thermal and spectroscopic studies of poly(N-vinyl pyrrolidone)/poly(vinyl alcohol) blend films, *J. Appl. Polym. Sci.* 114 (2009) 1202–1207, <https://doi.org/10.1002/app.30082>.
- [72] P. Yin, S. Hu, K. Qian, Z. Wei, L.-L. Zhang, Y. Lin, W. Huang, H. Xiong, W.-X. Li, H.-W. Liang, Quantification of critical particle distance for mitigating catalyst sintering, *Nat. Commun.* 12 (2021), 4865, <https://doi.org/10.1038/s41467-021-25116-2>.
- [73] Q. Liu, P. Rzepka, H. Frey, J. Tripp, A. Beck, L. Artiglia, M. Ranocchiari, J.A. van Bokhoven, Sintering behavior of carbon-supported Pt nanoparticles and the effect of surface overcoating, *Mater. Today Nano* 20 (2022), 100273, <https://doi.org/10.1016/j.mtnano.2022.100273>.
- [74] M. Gong, D. Xiao, Z. Deng, R. Zhang, W. Xia, T. Zhao, X. Liu, T. Shen, Y. Hu, Y. Lu, X. Zhao, H. Xin, D. Wang, Structure evolution of PtCu nanoframes from disordered to ordered for the oxygen reduction reaction, *Appl. Catal. B* 282 (2021), 119617, <https://doi.org/10.1016/j.apcatb.2020.119617>.
- [75] T.W. Hansen, A.T. DeLaRiva, S.R. Challa, A.K. Datye, Sintering of catalytic nanoparticles: particle migration or Ostwald ripening? *Acc. Chem. Res.* 46 (2013) 1720–1730, <https://doi.org/10.1021/ar3002427>.
- [76] S. Anantharaj, H. Sugime, S. Noda, Why shouldn’t double-layer capacitance (C_{dl}) be always trusted to justify Faradaic electrocatalytic activity differences? *J. Electroanal. Chem.* 903 (2021), 115842, <https://doi.org/10.1016/j.jelechem.2021.115842>.
- [77] Z. Yang, D. Yang, Y. Wang, Y. Long, W. Huang, G. Fan, Strong electrostatic adsorption-engaged fabrication of sub-3.0 nm PtRu alloy nanoparticles as synergistic electrocatalysts toward hydrogen evolution, *Nanoscale* 13 (2021) 10044–10050, <https://doi.org/10.1039/D1NR00936B>.
- [78] M. Li, H. Wang, W. Zhu, W. Li, C. Wang, X. Lu, RuNi nanoparticles embedded in N-doped carbon nanofibers as a robust bifunctional catalyst for efficient overall water splitting, *Adv. Sci.* 7 (2020), 1901833, <https://doi.org/10.1002/adv.201901833>.
- [79] Q. Liu, H. Meissel, I. Sadykov, S. Jones, N.V. Dijk, P. Rzepka, L. Artiglia, M. Ranocchiari, J.A. van Bokhoven, On the stability of Pt-based catalysts in HBr/Br₂ solution, *Helv. Chim. Acta* 104 (2021), e2100082, <https://doi.org/10.1002/hlca.202100082>.
- [80] X. Du, C. Zhang, H. Wang, Y. Wang, X. Zhang, Controlled synthesis of Co₉S₈@NiCo₂O₄ nanorod arrays as binder-free electrodes for water splitting with impressive performance, *J. Alloy. Compd.* 885 (2021), 160972, <https://doi.org/10.1016/j.jallcom.2021.160972>.
- [81] Y. Cao, T. Wang, X. Li, L. Zhang, Y. Luo, F. Zhang, A.M. Asiri, J. Hu, Q. Liu, X. Sun, A hierarchical CuO@NiCo layered double hydroxide core–shell nanoarray as an efficient electrocatalyst for the oxygen evolution reaction, *Inorg. Chem. Front.* 8 (2021) 3049–3054, <https://doi.org/10.1039/D1QI00124H>.
- [82] Z. Dai, X. Du, Y. Wang, X. Han, X. Zhang, Promoting urea oxidation and water oxidation through interface construction on a CeO₂@CoFe₂O₄ heterostructure, *Dalton Trans.* 50 (2021) 12301–12307, <https://doi.org/10.1039/D1DT01952J>.